

LA-UR-15-27790 (Accepted Manuscript)

Van Allen Probes observation and modeling of chorus excitation and propagation during weak geomagnetic activities

He, Y.; Xiao, F.; Zhou, Q.; Yang, C.; Liu, S.; Baker, D.; Kletzing, C.; Kurth, W.; Hospodarsky, G.; Spence, S.; Reeves, Geoffrey D.; Funsten, Herbert O.; Blake, J.

Provided by the author(s) and the Los Alamos National Laboratory (2016-01-28).

To be published in: JOURNAL OF GEOPHYSICAL RESEARCH-SPACE PHYSICS, Vol.120, iss.8, p.6371-6385, AUG 2015.

DOI to publisher's version: 10.1002/2015JA021376

Permalink to record: <http://permalink.lanl.gov/object/view?what=info:lanl-repo/lareport/LA-UR-15-27790>

Disclaimer:

Approved for public release. Los Alamos National Laboratory, an affirmative action/equal opportunity employer, is operated by the Los Alamos National Security, LLC for the National Nuclear Security Administration of the U.S. Department of Energy under contract DE-AC52-06NA25396. Los Alamos National Laboratory strongly supports academic freedom and a researcher's right to publish; as an institution, however, the Laboratory does not endorse the viewpoint of a publication or guarantee its technical correctness.

1 Van Allen Probes observation and modeling of
2 chorus excitation and propagation during weak
3 geomagnetic activities

Yihua He¹, Fuliang Xiao¹, Qinghua Zhou¹, Chang Yang¹, Si Liu¹, D. N.

Baker², C. A. Kletzing³, W. S. Kurth³, G. B. Hospodarsky³, H. E. Spence,⁴

G. D. Reeves⁵, H. O. Funsten⁶, J. B. Blake⁷

F. Xiao, School of Physics and Electronic Sciences, Changsha University of Science and Technology, Changsha, 410114, China. (flxiao@126.com)

¹School of Physics and Electronic

Abstract. We report correlated data on nightside chorus waves and energetic electrons during two small storm periods: 1 November 2012 ($Dst \approx -45$) and 14 January 2013 ($Dst \approx -18$). The Van Allen Probes simultaneously observed strong chorus waves at locations $L = 5.8 - 6.3$, with a

Sciences, Changsha University of Science
and Technology, Changsha, China

²Laboratory for Atmospheric and Space
Physics, University of Colorado, Boulder,
Colorado, USA

³Department of Physics and Astronomy,
University of Iowa, Iowa City, Iowa, USA

⁴Institute for the Study of Earth, Oceans,
and Space, University of New Hampshire,
Durham, New Hampshire, USA

⁵Space Science and Applications Group,
Los Alamos National Laboratory, Los
Alamos, New Mexico, USA

⁶ISR Division, Los Alamos National
Laboratory, Los Alamos, New Mexico, USA

⁷The Aerospace Corporation, Los
Angeles, California, USA

8 lower frequency band $0.1-0.5f_{ce}$ and a peak spectral density $\sim 10^{-4}$ nT²/Hz.
 9 In the same period, the fluxes and anisotropy of energetic ($\sim 10-300$ keV)
 10 electrons were greatly enhanced in the interval of large negative interplan-
 11 etary magnetic field B_z . Using a bi-Maxwellian distribution to model the ob-
 12 served electron distribution, we perform ray tracing simulations to show that
 13 nightside chorus waves are indeed produced by the observed electron distri-
 14 bution with a peak growth for a field-aligned propagation around between
 15 $0.3f_{ce}$ and $0.4f_{ce}$, at latitude $< 7^\circ$. Moreover, chorus waves launched with
 16 initial normal angles either $\theta < 90^\circ$ or $> 90^\circ$ propagate along the field ei-
 17 ther northward or southward, and then bounce back either away from Earth
 18 for a lower frequency or towards Earth for higher frequencies. The current
 19 results indicate that nightside chorus waves can be excited even during weak
 20 geomagnetic activities in cases of continuous injection associated with neg-
 21 ative B_z . Moreover, we examine a dayside event during a small storm C on
 22 8 May 2014 ($Dst \approx -45$) and find that the observed anisotropic energetic
 23 electron distributions potentially contribute to the generation of dayside cho-
 24 rus waves, but this requires more thorough studies in the future.

1. Introduction

Chorus-electron interaction controls local acceleration and loss of energetic electrons in Earth's radiation belts during different geomagnetic activities [*Summers et al.*, 1998, 2002; *Horne et al.*, 2005a, b; *Thorne*, 2010; *Thorne et al.*, 2013a; *Ding et al.*, 2013; *Su et al.*, 2014; *Xiao et al.*, 2009, 2010, 2014]. During the occurrence of enhanced seed electron injection, chorus waves become more efficient in accelerating radiation belts electrons to relativistic energies [*Yan et al.*, 2013; *Zhang et al.*, 2014]. Previous works have demonstrated that chorus waves are excited by anisotropic electrons with energies of a few keV ~ 100 keV in the low density plasma trough region [*Xiao et al.*, 1998, 2006; *Li et al.*, 2009; *Summers et al.*, 2009; *Jordanova et al.*, 2010] associated with substorm injection [*Meredith et al.*, 2001]. In-depth quantification of such chorus excitation requires simultaneous high-resolution observations of chorus spectra and electron distributions, but this was not available before the launch of the NASA Van Allen Probes on 30 August 2012 [*Mauk et al.*, 2012]. The Van Allen Probes have scientific instruments capable of collecting comprehensive particles and fields data throughout their orbit, with excellent detection sensitivity, energy resolution and temporal sampling capability. Relativistic (1 MeV \sim 20 MeV) or energetic (~ 10 -100 keV) electrons are detected by the Relativistic Electron-Proton Telescope (REPT) instrument [*Baker et al.*, 2012] or the Magnetic Electron Ion Spectrometer (MagEIS) [*Blake et al.*, 2013]. Hot (~ 1 eV to ~ 50 keV) particles are detected by the Helium Oxygen Proton Electron (HOPE) instrument [*Funsten et al.*, 2013] of the Energetic Particle, Composition and Thermal Plasma suite [*Spence et al.*, 2013]. Ions over the energy range from ~ 20 keV to ~ 1 MeV are measured by the Radiation Belt Storm

46 Probes Ion Composition Experiment (RBSPICE) [Mitchell *et al.*, 2013]. Electromagnetic
 47 waves are measured by the Electric and Magnetic Field Instrument Suite and Integrated
 48 Science (EMFISIS) Waves instrument [Kletzing *et al.*, 2013; Wygant *et al.*, 2013]. With
 49 aid of such scientific instruments, new advances have been made by the radiation belt
 50 community, including the discovery of a new radiation belt of relativistic electrons occur-
 51 ring between $L = 3$ and 3.5 [Baker *et al.*, 2013] associated with small hiss-driven pitch
 52 angle diffusion rates [Thorne *et al.*, 2013b], observation of extremely low-frequency (down
 53 to 20 Hz) plasmaspheric hiss waves in the outer plasmasphere [Li *et al.*, 2013], reconfirma-
 54 tion of in-situ acceleration in the heart of the radiation belts [Reeves *et al.*, 2013; Thorne
 55 *et al.*, 2013a], and the report of an impenetrable barrier to ultrarelativistic electrons at
 56 $L = 2.8$ [Baker *et al.*, 2014].

57 During two small storm periods: 1 November 2012 ($Dst \approx -45$) and 14 January 2013
 58 ($Dst \approx -18$), the MagEIS instrument observed substantial enhancements in differential
 59 fluxes (j) of energetic electrons with energies from ~ 10 -300 keV around the location
 60 $L = 6$. Meanwhile, the Waves instrument detected enhanced nightside chorus waves with
 61 frequencies from ~ 400 Hz up to ~ 5 kHz. These correlated data potentially suggest
 62 that the intensified nightside chorus waves can be excited by the enhanced distribution of
 63 anisotropic energetic electrons, but this needs in-depth data treatment and corresponding
 64 numerical simulation. Furthermore, we intend to study an event occurring on the dayside
 65 (> 10 MLT) during the small storm on 8 May 2014 ($Dst \approx -45$) to investigate whether
 66 the observed electron distribution can generate dayside chorus waves.

2. Correlated Van Allen Probe Data

We plot the time variation of the interplanetary magnetic field Bz (black) and geomagnetic activity Dst (red) (Figures 1a and 1h) and substorm activity AE index (Figures 1b and 1i) during storms A on 1 November 2012 and B on 13-14 January 2013. Storm A started at around 01:00 UT when Dst displayed a "dip" and then dropped rapidly down to -30 nT around 09:00 UT. A large negative Bz existed during the period 08:00-20:00 UT, allowing efficient coupling with the Earth's magnetosphere and prolonged geomagnetic activity. Meanwhile, AE remained a higher level (> 500 nT) and reached 1700 nT around 15:10 UT during the period 08:00-22:00 UT. Fluxes of energetic electrons in three channels (53.8, 79.8 and 108.3 keV) over a broad region $L = 3.5 - 6$ were greatly enhanced from 09:00 UT to 21:00 UT (Figure 1c-e). This indicates that continuous injection of electrons associated with negative Bz and higher AE occurred in the main phase when Dst continued to decrease to -62 nT around 21:00 UT (Figure 1a). Strong chorus waves primarily within the lower band $0.1 - 0.5f_{ce}$ (f_{ce} being the electron gyrofrequency) were observed from 08:00 UT to 13:00 UT, between $L = 3.4$ and 5.7 and 3.2 - 8.6 MLT by Van Allen Probe A (Figure 1f); $L = 3.5$ and 6.0 and 3.2 - 10.4 MLT by Probe B (Figure 1g). Chorus waves were also enhanced from 15:00-22:00 UT, covering $L = 3.5 - 5.8$ and 3.2 - 8.6 MLT detected by Probe A (Figure 1f); $L = 3.5 - 5.8$ and 3.2 - 10.4 MLT measured by Probe B (Figure 1g).

Storm B mainly consisted of a "two-step" main phase where Dst at first dropped from 10 nT rapidly down to -19 nT at 23:00 UT on January 13 and gradually increased back to -8 nT at 05:00 UT on January 14, and then dropped again down to -30 nT at 12:00 UT (Figure 1h). Bz displayed rapid fluctuations and alternatively changed signs. AE

remained a lower level (~ 100 nT) during the period 03:00-08:30 UT. Similarly, enhanced lower-band chorus waves were observed by Probe A (Figure 1m) and Probe B (Figure 1n) during three time periods 19:00-22:00 UT on January 13, 01:00-06:00 UT and 09:00-15:00 UT on January 14, with a wide range of spatial region: $L = 3.5 - 6.4$ and $3.2-9.3$ MLT. This corresponded to the occurrence of flux increases of energetic electrons in three channels (53.8, 79.8 and 108.3 keV) associated with continuous electron injection (Figure 1j-l).

In Figures 2-3, we show correlated data over a 40-minute period in storms A and B (corresponding to the pair of vertical lines in Figure 1) including electron pitch angle distributions collected by the MagEIS instrument, wave magnetic spectral intensity, wave normal angle and wave ellipticity from the Waves instrument. Fluxes of energetic electrons maximized at 90° and dropped substantially at small pitch angles, indicating that an electron anisotropy and source of free energy are available for exciting chorus waves. Consequently, strong chorus waves occurred in the aforementioned periods, with low wave normal angles and a low (ellipticity ≈ 1) degree of elliptical polarization, implying that chorus waves propagate almost along the ambient magnetic field direction [*Horne et al.*, 2007]. Moreover, chorus waves had stronger intensity and broader frequency extent in the period of 09:00-09:50 UT on November 1, 2012 (Figure 2) than in the period of 03:00-03:40 UT on January 14, 2013 (Figure 3), due to a slightly higher anisotropy and number density of energetic electrons in the former period.

3. Numerical Modeling

3.1. Modeling Method

Here, we focus on the storm-time periods as shown in Figures 2-3 when excited chorus waves and enhancements in fluxes and anisotropy of energetic electrons were simultaneously observed by Van Allen Probes A and B. We utilize a previously developed ray-tracing program [Xiao *et al.*, 2007], which follows the methodology of the HOTRAY code [Horne, 1989], to obtain chorus position at each time step by integrating Hamilton's equations [Horne, 1989; Suchy., 1981].

Similar to previous works [Horne, 1989; Chen *et al.*, 2010; Xiao *et al.*, 2012], we define a local Cartesian system, in which the z axis points along the ambient magnetic field line, the x axis orthogonal to the z axis lies in the meridian plane and points away from Earth at the equator, and the y axis completes the righthanded set. The wave normal angle θ is the angle between the wave vector \mathbf{k} and the z axis. The wave azimuthal angle η is the angle between \mathbf{k}_\perp (the projection of \mathbf{k} onto the xy plane) and the x axis. In particular, $\eta = 0^\circ, 90^\circ, 180^\circ$ and 270° indicate \mathbf{k}_\perp pointing away from Earth, toward later MLT (eastward), toward Earth, and toward earlier MLT (westward), respectively.

Here, we use a dipole magnetic field model and a recently constructed and concise plasma density (N_e) model [Chen *et al.*, 2012]:

$$N_e = N_i + N_{ps}(1 - g(L)) + N_{tr}g(L), \quad (1)$$

here, N_i , N_{ps} , and N_{tr} respectively stand for densities of the ionosphere, the plasmasphere and the trough; $g(L)$ represents the transition function in controlling the plasmasphere shape (the transition from the plasmasphere to the plasma trough). Explicit expressions for those aforementioned terms are written by equations (2-4) in the previous

work [Chen et al., 2012]. In the following, we use those equations to calculate the ambient densities (N_e) in different regions of L -shells and MLT. Then those obtained values of N_e are used to evaluate the chorus wave growth.

Wave instability occurs during the gyroresonance between chorus and electrons. At every step of the ray path, we calculate the local chorus wave growth rate γ (the imaginary part of wave frequency). Then we obtain the path-integrated wave gain in dB by integrating the local growth rate along the ray path:

$$\text{Gain} = 20 \log_{10} \left(\exp \left(\int \gamma dt \right) \right) \quad (2)$$

The phase space density (PSD) f of energetic electrons is fitted with a sum of five-species bi-Maxwellian distribution $f = \sum_i f_i$, with f_i as a function of parallel ($v_{\parallel i}$) and perpendicular ($v_{\perp i}$) velocity being written by:

$$f_i(v_{\parallel i}, v_{\perp i}) = \frac{n_{hi}}{\pi^{3/2} \theta_{\perp i}^2 \theta_{\parallel i}} \exp \left(-\frac{v_{\parallel i}^2}{\theta_{\parallel i}^2} - \frac{v_{\perp i}^2}{\theta_{\perp i}^2} \right). \quad (3)$$

Here, n_{hi} is the number density of each species; $\theta_{\perp i}$ and $\theta_{\parallel i}$ denote the perpendicular and parallel thermal velocities of each species associated with the thermal temperature respectively by $2\theta_{\perp i}^2 = m_e T_{\perp i}$ and $2\theta_{\parallel i}^2 = m_e T_{\parallel i}$, with m_e being the electron mass.

3.2. Modeling for Storm A

Using the conversion $j = p^2 f$ and comparing the data from the MagEIS instrument, we show the fits of electron distributions at two specific times 09:24 UT (Figure 4a) and 09:40 UT (Figure 4c) on 1 November, 2012, with the corresponding fitting parameters shown in Table 1. It is shown that electron anisotropy starts to occur above 10 keV and becomes significant above 100 keV. The corresponding local growth rates scaled by the angular gyrofrequency Ω_{ce} (γ/Ω_{ce}) for different initial wave normal angles (θ_0) are

plotted in Figure 4b for 09:24 UT and Figure 4d for 09:40 UT. Local growth of chorus peaks between 0.35 and $0.37f_{ce}$ and drops rapidly as θ_0 increases in both cases due to the concurrence of Landau damping and higher harmonic cyclotron resonances, consistent with observations. In particular, for $\theta_0 = 0^\circ$, γ/Ω_{ce} can approach 1.55×10^{-3} at 09:24 UT and 7.5×10^{-4} at 09:40 UT, respectively.

It should be mentioned that Probe B observed upper-band chorus emissions around 09:40 UT. Based on the linear treatment of wave growth, the chorus frequency range tends to scale with the anisotropy of energetic electrons [Xiao *et al.*, 1998; Summers *et al.*, 2009]. The observed upper-band chorus emissions appear to be associated with the higher anisotropy of energetic electrons which were not observed by Probe B in the same period. This is probably because wave growth is basically associated with pitch angle scattering to smaller pitch angles and a reduction in anisotropy of electrons [Gendrin, 1981]. In general, wave growth occurs very rapidly, allowing the higher anisotropy of energetic electrons more difficult to be observed.

Due to the brief duration of the UT interval and limited latitudinal coverage of the Van Allen Probes, we assume that the anisotropy and flux of energetic electrons remain unchanged during chorus propagation. Then, we demonstrate variations of the path integrated gain and wave normal angle with time for different frequencies and initial wave normal angles (θ_0) based on the data from Probes A (Figure 5) and B (Figure 6). Correspondingly, wave path gain is highest for $\theta_0 = 0^\circ$ in all the cases due to the highest local growth rate, reaching a maximum value 75dB at $0.3f_{ce}$ (Figure 5b). Furthermore, path gain increases at first to the maximum around $t = 0.1 - 0.2$ s for θ_0 decreasing from 20° to 0° (corresponding to the latitude $\lambda \leq 7^\circ$) and then drops significantly with

time (Figures 5a-c and 6a-c). This is because the local growth rate is positive from the beginning to $t = 0.1 - 0.2$ s, leading to a continuously increasing path gain (see (2)). This can explain the previous statistical results that chorus waves in the night-to-morning section are most intense within the latitude $\lambda \approx 15^\circ$ [Shprits et al., 2007; Li et al., 2007, 2009]. After 0.2 s, as the wave normal angle increases rapidly with time (Figures 5d-f and 6d-f), both Landau damping and some higher harmonic cyclotron resonances dominate over the wave growth. As a result, the chorus growth rate becomes negative and the corresponding path gain decreases. The results above confirm again that field aligned propagating chorus waves reach the maximum growth rate.

In Figure 7, we plot the ray paths of chorus launched at the locations $L = 5.8$ for Probe A and $L = 6.0$ for Probe B, with different wave frequencies and initial wave normal angles ($\theta_0 < 90^\circ$). Clearly, chorus waves are found to propagate northward basically along the field line (dotted) and reflect at high latitude. This provides a reasonable explanation for the observation that excited chorus waves occurred in the northward region ($\lambda > 0^\circ$) (Figure 2). Electromagnetic wave reflection in the magnetosphere takes place where the component of wave group velocity along the ambient magnetic field is reversed. As analyzed in detail by Helliwell [1969], the reflection for whistler-mode waves generally occurs around the local lower hybrid resonance frequency $f_{LH} = \sqrt{f_{ce}f_{ci}}$ (f_{ci} being the ion gyrofrequency), which is essentially due to the closing of the refractive index surface at f_{LH} . Based on Snell's law, the ray path tends to swing around and reverses its direction near f_{LH} . Considering that f_{LH} is proportional to the local ambient magnetic field, lower frequency ($0.2f_{ce}$) chorus waves propagate upward and reflect at higher L -shells, downward away from Earth (Figures 7a and 7d). Higher frequency (between 0.3

and $0.35f_{ce}$) chorus waves travel upward and reflect at lower L -shells, downward towards Earth (Figures 7b-c and 7e-f).

3.3. Modeling for Storm B

Here, we model the electron PSDs at the two indicated times 03:13 UT and 03:33 UT on 14 January, 2013, with data from Probes A (Figure 8a) and B (Figure 8c), respectively. The fitting parameters are shown in Table 2. Clearly, distinct electron anisotropy occurs above 100 keV but the anisotropy is lower than that in storm A, due to the lower level of geomagnetic activity in storm B (see Figure 1). Using the fitting parameters in Table 2, we calculate the local growth rate for different initial wave normal angles ($\theta_0 > 90^\circ$) and show the results in the lower panels of Figure 8. Chorus has a maximum local growth rate around $0.35f_{ce}$ but the growth rate at each wave normal angle is smaller than that in storm A because of the slightly lower anisotropy and number density of energetic electrons measured by each Probe in storm B (see Tables 1 and 2). Specifically, in the antiparallel direction $\theta_0 = 180^\circ$, $\gamma/\Omega_{ce} \approx 4 \times 10^{-4}$ at 03:13 UT and 4.5×10^{-4} at 03:33 UT, respectively. As chorus propagation becomes more oblique, i.e., θ_0 deviating more away from 180° , the local growth rate becomes smaller, which is analogous to the situation in storm A.

We plot the path integrated gain and wave normal angle as a function of propagation time for different frequencies and initial wave normal angles (θ_0) in Figures 9 and 10 by using the data from Probes A and B, respectively. The wave path gain becomes largest in the antiparallel ($\theta_0 = 180^\circ$) propagation in all cases, with a peak value 28dB at $0.3f_{ce}$ (Figure 9b). The wave normal angle for each initial θ_0 decreases away from 180° (towards more oblique) all the time. Furthermore, the path gain first increases due to the accumulated positive growth rate along the ray path, reaches a peak around $|\lambda| \approx 6^\circ$

216 and then drops rapidly due to the negative growth rate associated with the wave normal
217 angle increasing with time.

218 Figure 11 illustrates how chorus waves with different wave frequencies and initial normal
219 angles ($\theta_0 > 90^\circ$) propagate in the magnetosphere. Starting at locations either at $L = 6.3$
220 for Probe A or $L = 6.1$ for Probe B, chorus waves travel southward (in contrast to the
221 northward propagation in storm A) basically along the field line and encounters reflection
222 at the high latitude where the field-aligned component of wave group velocity reverses its
223 direction. This can account for the observation that strong chorus waves are observed in
224 the southward region ($\lambda < 0^\circ$) (Figure 3). For the lower frequency $0.2f_{ce}$ all those chorus
225 waves bounce back away from Earth (Figures 11a and 11d). For higher frequency between
226 0.3 and $0.35f_{ce}$, those chorus waves travel towards Earth (Figures 11b-c and 11e-f).

227 It should be mentioned that the bi-Maxwellian distribution doesn't appear to fit very
228 well the observed electron distribution above ~ 60 keV in Figures 4 and 8, primarily due
229 to the big difficulty in allowing a good fit at each value of energy in cases of interest.
230 This should affect the result of linear growth rate calculation. We have made a rough
231 check (not shown for brevity) in choosing slightly different parameters to allow a better
232 fit above ~ 60 keV but a worse fit in other energies. We find that the worst case produces
233 the reduction in the peak growth rate by $\sim 40\%$ for $\theta_0 = 0^\circ$ at 09:24 UT in storm A but
234 no big differences in all other cases.

235 Moreover, we have checked the EMFISIS upper hybrid resonance band [*Kurth et al.*,
236 2015] and found that the adopted density is comparable to the in-situ density in the
237 simulation period. We have also inferred the plasmopause location from the EMFISIS
238 upper hybrid resonance band and found that the plasmopause roughly lies in $L = 4 - 4.5$.

However, more works are still needed in the future due to some uncertainties in accurate determination of the upper hybrid resonance frequency [Kurth *et al.*, 2015].

3.4. Modeling for Storm C

Here, we shall analyze an event observed on the dayside (> 10 MLT) during the small storm on 8 May 2014 ($Dst \approx -45$) to see whether the observed electron distribution is sufficient to generate dayside chorus waves. The time variations of IMF Bz (black), Dst index (red) and AE index are shown in Figure 12a-b, in which Dst dropped down to -45 around 08:00 UT and a large negative Bz lasted roughly from 00:00 to 07:40 UT. AE roughly increased from 00:00 to 09:00 UT and rapidly up to 1314 nT around 09:40 UT. The large negative Bz and higher AE are favorable for maintaining electron injection from the plasmasheet, leading to increase in anisotropy of energetic electrons. Then those anisotropic energetic electrons drift westward around Earth, potentially causing chorus growth on the dayside. The pair of vertical lines indicate the simulation periods: 09:50-10:30 UT when an increase in pitch angle anisotropy of energetic electrons and enhanced chorus wave magnetic spectral intensity are observed by Probe B (Figure 12c-d). Lower band ($0.1 - 0.5f_{ce}$) chorus waves with a peak spectral density $\sim 10^{-5}$ nT²/Hz stayed at $L = 4.8 - 5.3$ and $10.9 - 11.5$ MLT, with small wave normal angles and a small (ellipticity ≈ 1) degree of elliptical polarization (Figure 12e-f).

We model the electron PSDs at the two indicated times 10:00 UT (Figure 13a) and 10:08 UT (Figure 13c), with the corresponding fitting parameters shown in Table 3. Electron anisotropy becomes noticeable above 10 keV and significant above 100 keV. The corresponding scaled local growth rates γ/Ω_{ce} for different initial wave normal angles θ_0 are shown in Figure 13b for 10:00 UT and Figure 13d for 10:08 UT. Local growth maximizes

between 0.28 and $0.32f_{ce}$, decreasing rapidly with increasing θ_0 in both cases because of the contribution of Landau damping and higher harmonic cyclotron resonances, consistent with observations. Specifically, in the case of $\theta_0 = 0^\circ$, γ/Ω_{ce} can approach 0.7×10^{-4} at 10:00 UT and 1.8×10^{-4} at 10:08 UT, respectively. This result suggests that the observed electron distributions potentially contribute to the generation of dayside chorus waves in this event. However, the simulated linear growth rate of the dayside chorus is smaller than that of the nightside chorus and probably below the detectable intensity level, partially because of the much lower number density of energetic electrons which provide a source of free energy for chorus excitation. This appears to suggest that other mechanisms may be needed to explain the relatively strong chorus observed on the dayside.

4. Summary

We have provided simultaneous observation of nightside chorus waves and energetic electrons measured by Van Allen Probes during two small storm periods A and B: 1 November 2012 ($Dst \approx -45$) and 14 January 2013 ($Dst \approx -18$). Strong chorus waves stayed near $L = 5.8 - 6.3$ with a lower frequency band $0.1 - 0.5f_{ce}$ and a peak spectral density $\sim 10^{-4}$ nT²/Hz. Meanwhile, enhancements in fluxes and anisotropies of energetic (~ 10 -300 keV) electrons are observed in the interval of large negative interplanetary magnetic field Bz , leading to intensified chorus waves. In order to reveal the inherent correlation between excited chorus and increases in electron fluxes and anisotropy, we adopt a bi-Maxwellian distribution to model the observed electron distributions, and then perform ray tracing simulations to show that chorus waves are indeed produced by the observed electron distribution. In the case of parallel or antiparallel propagation, the local growth rate γ/Ω_{ce} and corresponding path gain can reach the maximum values of 1.55×10^{-3} and

75dB in the storm A; 4.5×10^{-4} and 28dB in the storm B, respectively. In particular, we have examined a dayside event during a small storm C on 8 May 2014 ($Dst \approx -45$) when lower band ($0.1 - 0.5f_{ce}$) chorus waves occurred at $L = 4.8 - 5.3$ and $10.9 - 11.5$ MLT. We have shown that the observed anisotropic energetic electron distributions are possible for generating dayside chorus waves. The main conclusions can be summarized as follows.

1. Local growth rates of nightside chorus waves peak between $0.35-0.37f_{ce}$ and drop rapidly when the initial wave normal angle θ_0 increases due to the concurrence of Landau damping and higher harmonic cyclotron resonances. Moreover, the growth rate and the corresponding path gain are higher in storm A than those in storm B due to higher fluxes and anisotropies of energetic electrons associated with the larger Bz and higher AE in storm A.

2. Nightside chorus path gain becomes largest for $\theta_0 = 0^\circ$ (parallel) or 180° (antiparallel) because of the highest local growth rate in cases of interest. The path gain increases at first due to the accumulated positive growth rate along the ray path, reaches a maximum within a few degrees near the equator and then drops rapidly due to the negative growth rate as the wave normal angle increases with time. This can give a reasonable explanation for the previous statistical results that the night-to-morning section chorus waves are most intense within $\lambda \approx 15^\circ$.

3. Nightside chorus ray paths with initial normal angle either $\theta_0 < 90^\circ$ or $> 90^\circ$ travel along the field either northward or southward, providing a reasonable explanation for the observation that strong chorus waves occur either in the latitude $\lambda > 0$ (storm A) or < 0 (storm B). Then they bounce back either away from Earth for a lower frequency or towards Earth for higher frequencies. These results above indicate that chorus waves can

be excited even during weak geomagnetic activities if continuous electron injection occurs associated with the negative Bz or higher AE .

4. Local growth rates (γ/Ω_{ce}) of dayside chorus waves maximizes between 0.28 and $0.32f_{ce}$, decreasing rapidly with increasing θ_0 because of the contribution of Landau damping and higher harmonic cyclotron resonances, consistent with observations. Moreover, for $\theta_0 = 0^\circ$, γ/Ω_{ce} can approach 1.8×10^{-4} , suggesting that the observed anisotropic energetic electron distributions potentially contribute to the generation of dayside chorus waves in this event. However, the calculated chorus growth rate on the dayside is lower than that on the nightside and probably below the detectable intensity level. This tends to suggest that additional mechanisms are probably required to explain the relatively strong chorus waves observed on the dayside.

Acknowledgments. This work is supported by the National Natural Science Foundation of China grants 41404130, 41274165, 41204114, the Aid Program for Science and Technology Innovative Research Team in Higher Educational Institutions of Hunan Province, and the Construct Program of the Key Discipline in Hunan Province. All the Van Allen Probes data are publicly available at <https://emfisis.physics.uiowa.edu/data/index> by the EMFISIS suite and at http://www.rbsp-ect.lanl.gov/data_pub/ by the REPT and MagEIS instrument. The OMNI data are obtained from <http://omniweb.gsfc.nasa.gov/form/dx1.html>. This work was also supported from JHU/APL contract No. 921647 and 967399 under NASA Prime contract No. NAS5-01072.

References

- Baker, D. N., et al. (2012), The relativistic electron-proton telescope (REPT) instrument on board the Radiation Belt Storm Probes (RBSP) spacecraft: Characterization of Earth's radiation belt high-energy particle populations, *Space Sci. Rev.*, doi:10.1007/s11214-012-9950-9.
- Baker, D. N., et al. (2013), A long-lived relativistic electron storage ring embedded in Earth's outer Van Allen belt, *Science*, *340*, 186–190, doi:10.1126/science.1233518.
- Baker, D. N., et al. (2014), An impenetrable barrier to ultrarelativistic electrons in the Van Allen radiation belts, *Nature*, *515*, 531–539, doi:10.1038/nature13956.
- Blake, J. B., et al. (2013), The magnetic electron ion spectrometer (MagEIS) instruments aboard the radiation belt storm probes (RBSP) spacecraft, *Space. Sci. Rev.*, doi:10.1007/s11214-013-9991-8.
- Chen, L., R. M. Thorne, V. K. Jordanova, and R. B. Horne (2010), Global simulation of magnetosonic waves instability in the storm time magnetosphere, *J. Geophys. Res.*, *115*, A11,222, doi:10.1029/2010JA015707.
- Chen, L., J. Bortnik, W. Li, R. M. Thorne, and R. B. Horne (2012), Modeling the properties of plasmaspheric hiss: 1. Dependence on chorus wave emission, *J. Geophys. Res.*, *117*, A05,201, doi:10.1029/2011JA017201.
- Ding, Y., Z. He, Z. Zhang, and F. Xiao (2013), Influence of wave normal angle on gyroresonance between chorus waves and outer radiation belt electrons, *Sci. China Tech. Sci.*, *56*, 2681–2689, doi:10.1007/s11431-013-5363-6.
- Funsten, H. O., et al. (2013), Helium, Oxygen, Proton, and Electron (HOPE) Mass Spectrometer for the Radiation Belt Storm Probes Mission, *Space Sci. Res.*, *259*, doi:

10.1007/s11214-013-9968-7.

Gendrin, R. (1981), General relationships between wave amplification and particle diffusion in a magnetoplasma, *Rev. Geophys. Space Phys.*, *19*, 171.

Helliwell, R. A. (1969), Low-Frequency Waves in the Magnetosphere, *Rev. Geophys.*, *7*, 281–303.

Horne, R. B. (1989), Integrated growth of electrostatic waves: The generation of terrestrial myriametric radiation, *J. Geophys. Res.*, *94*, 8895.

Horne, R. B., R. M. Thorne, S. A. Glauert, J. M. Albert, N. P. Meredith, and R. R. Anderson (2005a), Timescale for radiation belt electron acceleration by whistler mode chorus waves, *J. Geophys. Res.*, *110*, A03,225, doi:10.1029/2004JA010811.

Horne, R. B., et al. (2005b), Wave acceleration of electrons in the Van Allen radiation belts, *Nature*, *437*, 227, doi:10.1038/nature03939.

Horne, R. B., R. M. Thorne, S. A. Glauert, N. P. Meredith, D. Pokhotelov, and O. Santolík (2007), Electron acceleration in the Van Allen radiation belts by fast magnetosonic waves, *Geophys. Res. Lett.*, *34*, L17,107, doi:10.1029/2007GL030267.

Jordanova, V. K., R. M. Thorne, W. Li, and Y. Miyoshi (2010), Excitation of whistler-mode chorus from global ring current simulations, *J. Geophys. Res.*, *115*, A00F10, doi:10.1029/2009JA014810.

Kletzing, C. A., et al. (2013), The Electric and Magnetic Field Instrument Suite and Integrated Science (EMFISIS) on RBSP, *Space Sci. Rev.*, doi:10.1007/s11214-013-9993-6.

Kurth, W. S., S. D. Pascuale, J. B. Faden, C. A. Kletzing, G. B. Hospodarsky, S. Thaller, and J. R. Wygant (2015), Electron densities inferred from plasma wave spectra obtained

by the Waves instrument on Van Allen Probes, *J. Geophys. Res. Space Physics*, *120*, 904–914, doi:10.1002/2014JA020857.

Li, W., Y. Y. Shprits, and R. M. Thorne (2007), Dynamic evolution of energetic outer zone electrons due to wave-particle interactions during storms, *J. Geophys. Res.*, *112*, A10,220, doi:10.1029/2007JA012368.

Li, W., et al. (2009), Global distribution of whistler-mode chorus waves observed on the THEMIS spacecraft, *Geophys. Res. Lett.*, *36*, L09,104, doi:10.1029/2009GL037595.

Li, W., et al. (2013), An unusual enhancement of low-frequency plasmaspheric hiss in the outer plasmasphere associated with substorm-injected electrons, *Geophys. Res. Lett.*, *40*, 1–6, doi:10.1002/grl.50787.

Mauk, B. H., N. J. Fox, S. G. Kanekal, R. L. Kessel, D. G. Sibeck, and A. Ukhorskiy (2012), Science Objectives and Rationale for the Radiation Belt Storm Probes Mission, *Space Sci. Rev.*, pp. 1–15, doi:10.1007/s11214-012-9908-y.

Meredith, N. P., R. B. Horne, and R. R. Anderson (2001), Substorm dependence of chorus amplitudes: Implications for the acceleration of electrons to relativistic energies, *J. Geophys. Res.*, *106*, 13,165.

Mitchell, D. J., et al. (2013), Radiation Belt Storm Probes Ion Composition Experiment (RBSPICE), *Space Sci. Rev.*, doi:10.1007/s11214-013-9965-x.

Reeves, G. D., et al. (2013), Electron acceleration in the heart of the Van Allen radiation belts, *Science*, *341*, 991–994, doi:10.1126/science.1237743.

Shprits, Y. Y., N. P. Meredith, and R. M. Thorne (2007), Parameterization of radiation belt electron loss timescales due to interactions with chorus waves, *Geophys. Res. Lett.*, *34*, L11,110, doi:10.1029/2006GL029050.

- 395 Spence, H. E., et al. (2013), Science Goals and Overview of the Energetic Particle, Com-
396 position, and Thermal Plasma (ECT) Suite on NASAs Radiation Belt Storm Probes
397 (RBSP) Mission, *Space Sci. Rev.*, *179*, 311–336, doi:10.1007/s11214-013-0007-5.
- 398 Su, Z., et al. (2014), Nonstorm time dynamics of electron radiation belts observed by the
399 van allen probes, *Geophys. Res. Lett.*, *41*, 229–235, doi:10.1002/2013GL058912.
- 400 Suchy., K. (1981), Real Hamilton equations of geomagnetic optics for media with moderate
401 absorption, *Radio Sci.*, *16*, 1179.
- 402 Summers, D., R. M. Thorne, and F. Xiao (1998), Relativistic theory of wave-particle
403 resonant diffusion with application to electron acceleration in the magnetosphere, *J.*
404 *Geophys. Res.*, *103*, 20,487.
- 405 Summers, D., C. Ma, N. P. Meredith, R. B. Horne, R. M. Thorne, D. Heynderickx, and
406 R. R. Anderson (2002), Model of the energization of outer-zone electrons by whistler-
407 mode chorus during the october 9, 1990 geomagnetic storm, *Geophys. Res. Lett.*, *29*(24),
408 2174, doi:10.1029/2002GL016039.
- 409 Summers, D., R. Tong, and R. M. Thorne (2009), Limit on stably trapped particle fluxes in
410 planetary magnetospheres, *J. Geophys. Res.*, *114*, A10,210, doi:10.1029/2009JA014428.
- 411 Thorne, R. M. (2010), Radiation belt dynamics: The importance of wave-particle inter-
412 actions, *Geophys. Res. Lett.*, *37*, L22,107, doi:10.1029/2010GL044990,.
- 413 Thorne, R. M., et al. (2013a), Rapid local acceleration of relativistic radiation-belt elec-
414 trons by magnetospheric chorus, *Nature*, *504*, 411–414, doi:10.1038/nature12889.
- 415 Thorne, R. M., et al. (2013b), Evolution and slow decay of an unusual narrow ring of rel-
416 ativistic electrons near $L \sim 3.2$ following the September 2012 magnetic storm, *Geophys.*
417 *Res. Lett.*, *40*, 3507–3511, doi:10.1002/grl.50627.

- 418 Wygant, J. R., et al. (2013), The Electric Field and Waves (EFW) instruments on the
419 Radiation Belt Storm Probes Mission, *Space Sci. Rev.*, doi:10.1007/s1124-013-0013-7.
- 420 Xiao, F., R. M. Thorne, and D. Summers (1998), Instability of electromagnetic R-mode
421 waves in a relativistic plasma, *Phys. Plasmas*, 5, 2489.
- 422 Xiao, F., Q. H. Zhou, H. Y. He, and L. J. Tang (2006), Instability of whistler-mode waves
423 by a relativistic kappa-loss-cone distribution in space plasmas, *Plasma Phys. Controlled
424 Fusion*, 48, 1437, doi:10.1088/0741-3335/48/9/012.
- 425 Xiao, F., L. Chen, H. N. Zheng, and S. Wang (2007), A parametric ray tracing study of
426 superluminous auroral kilometric radiation wave modes, *J. Geophys. Res.*, 112, A10,214,
427 doi:10.1029/2006JA012178.
- 428 Xiao, F., Z. Su, H. Zheng, and S. Wang (2009), Modeling of outer radiation belt
429 electrons by multidimensional diffusion process, *J. Geophys. Res.*, 114, A03,201, doi:
430 10.1029/2008JA013580.
- 431 Xiao, F., Z. Su, H. Zheng, and S. Wang (2010), Three-dimensional simulations of outer
432 radiation belt electron dynamics including cross diffusion terms, *J. Geophys. Res.*, 115,
433 A05,216, doi:10.1029/2009JA014541.
- 434 Xiao, F., Q. Zhou, Z. He, and L. Tang (2012), Three-dimensional ray tracing of fast
435 magnetosonic waves, *J. Geophys. Res.*, 117, A06,208, doi:10.1029/2012JA017589.
- 436 Xiao, F., et al. (2014), Chorus acceleration of radiation belt relativistic electrons during
437 March 2013 geomagnetic storm, *J. Geophys. Res. Space Physics*, 119, 3325–3332, doi:
438 10.1002/2014JA019822.
- 439 Yan, Q., L. Shi, and S. Liu (2013), Effect of seed electron injection on chorus-driven
440 acceleration of radiation belt electrons, *Sci. China. Tech. Sci.*, 56, 492–498.

441 Zhang, Y., H. Zhu, L. Zhang, Y. He, Z. Gao, Q. Zhou, C. Yang, and F. Xiao (2014),
442 Effect of low energy electron injection on storm-time evolution of radiation belt en-
443 ergetic electrons: three-dimensional modeling, *Astrophys. Space Sci.*, *352*, 613–620,
444 doi:10.1007/s10509-014-1984-x.

Table 1. Parameters for the electron distribution in storm A

09:24 UT, Probe A, $L = 5.8$				09:40 UT, Probe B, $L = 6.0$		
Species	$n_h(\text{cm}^{-3})$	$T_{\parallel} \text{ (eV)}$	$T_{\perp} \text{ (eV)}$	$n_h(\text{cm}^{-3})$	$T_{\parallel} \text{ (eV)}$	$T_{\perp} \text{ (eV)}$
1	2.8	1.5×10^1	1.5×10^1	1.6	1.2×10^1	1.2×10^1
2	0.41	2.1×10^2	2.1×10^2	0.41	7.9×10^1	1.1×10^2
3	0.7	1.8×10^3	1.8×10^3	0.33	5.2×10^2	9.8×10^2
4	0.3	3.5×10^3	5.5×10^3	0.53	3.9×10^3	6.1×10^3
5	0.15	9.2×10^3	1.7×10^4	0.052	1.2×10^4	2.1×10^4

Table 2. Parameters for the electron distribution in storm B

03:13 UT, Probe A, $L = 6.3$				03:33 UT, Probe B, $L = 6.1$		
Species	$n_h(\text{cm}^{-3})$	$T_{\parallel} \text{ (eV)}$	$T_{\perp} \text{ (eV)}$	$n_h(\text{cm}^{-3})$	$T_{\parallel} \text{ (eV)}$	$T_{\perp} \text{ (eV)}$
1	2.6	1.4×10^1	1.4×10^1	2.1	1.4×10^1	1.4×10^1
2	0.31	1.9×10^2	1.9×10^2	0.32	1.5×10^2	2.1×10^2
3	0.58	2.5×10^3	3.2×10^3	0.38	1.7×10^3	3.2×10^3
4	0.51	3.5×10^3	4.3×10^3	0.21	3.5×10^3	3.9×10^3
5	0.1	8.5×10^3	1.4×10^4	0.048	1.2×10^4	2.0×10^4

Table 3. Parameters for the electron distribution in storm C

10:00 UT, Probe B, $L = 5.2$				10:08 UT, Probe B, $L = 5.1$		
Species	$n_h(\text{cm}^{-3})$	$T_{\parallel} \text{ (eV)}$	$T_{\perp} \text{ (eV)}$	$n_h(\text{cm}^{-3})$	$T_{\parallel} \text{ (eV)}$	$T_{\perp} \text{ (eV)}$
1	0.65	1.1×10^1	1.4×10^1	0.76	1.2×10^1	1.3×10^1
2	0.18	7.5×10^1	8.5×10^1	0.21	7.2×10^1	8.7×10^1
3	0.065	1.6×10^2	2.1×10^2	0.063	1.4×10^2	2.1×10^2
4	0.076	4.8×10^2	5.2×10^2	0.051	5.1×10^2	6.2×10^2
5	0.038	1.55×10^4	2.35×10^4	0.035	1.8×10^4	2.9×10^4

Figure 1. Van Allen Probe data during 1 November 2012 (left) and 13-14 January 2013 (right). (a, h) The IMF Bz (black) and the Dst index (red). (b, i) The AE index. (c-e, j-l) Flux of energetic electrons measured by ECT-MagEIS instrument onboard Probes A and B. (f-g, m-n) Wave magnetic field spectral density (in unit of \log_{10}) measured by EMFISIS instrument onboard Probes A and B. The white lines obtained by the EMFISIS magnetic field data represent $0.1f_{ce}$ (solid), $0.5f_{ce}$ (dashed) and f_{ce} (dot-dashed). The pair of vertical lines indicate the simulation periods: 09:10-09:50 UT on 1 November 2012 and 03:00-03:40 UT on 14 January 2013.

Figure 2. Data collected by Probes A (left) and B (right) during 09:10-09:50 UT on 1 November 2012. (a, e) Pitch angle distributions of energetic (53.8-108.3 keV) electron fluxes in unit of \log_{10} . (b, f) wave magnetic field spectral density (in unit of \log_{10}). The white lines represent $0.1f_{ce}$ (solid), $0.5f_{ce}$ (dashed) and f_{ce} (dot-dashed). (c, g) Wave normal angle. (d, h) Wave ellipticity.

Figure 3. The same as Figure 2 except during 03:00-03:40 UT on 14 January 2013.

Figure 4. (upper) Modeled bi-Maxwellian distribution (solid) to the observed electron PSD (discrete) for $v_{\perp} = 0$ (blue) and $v_{\parallel} = 0$ (red). (lower) The corresponding local growth rate γ scaled by the electron gyrofrequency Ω_{ce} as a function of wave frequency ω at the initial azimuthal angle $\eta = 0^{\circ}$ and different initial wave normal angles (θ_0).

Figure 5. Variations of path-integrated gain (left) and the wave normal angle (right) for different wave frequencies and initial wave normal angles (shown) with time t based on the data from Probe A.

Figure 6. The same as Figure 5 but for Probe B.

Figure 7. Ray paths for different wave parameters (shown). The pentagrams indicate the source locations at $L = 5.8$ and 6.0 for Probes A and B. Also shown are the plasma-pause (dashed), and field lines (dotted) with the invariant latitudes (or L): 63° (4.85), 65° (5.6) and 67° (6.55). $f_{LH} \approx 93$ and 103 Hz at the equator $L = 6$ and 5.8 .

Figure 8. (upper) Modeled bi-Maxwellian distribution (solid) to the observed electron PSD (discrete) for $v_\perp = 0$ (blue) and $v_\parallel = 0$ (red). (lower) The corresponding scaled local growth rate at the initial azimuthal angle $\eta = 0^\circ$ and different initial wave normal angles (θ_0).

Figure 9. Variations of path-integrated gain (left) and the wave normal angle (right) for different wave frequencies and initial wave normal angles (shown) with time t based on the data from Probe A.

Figure 10. The same as Figure 9 but for Probe B.

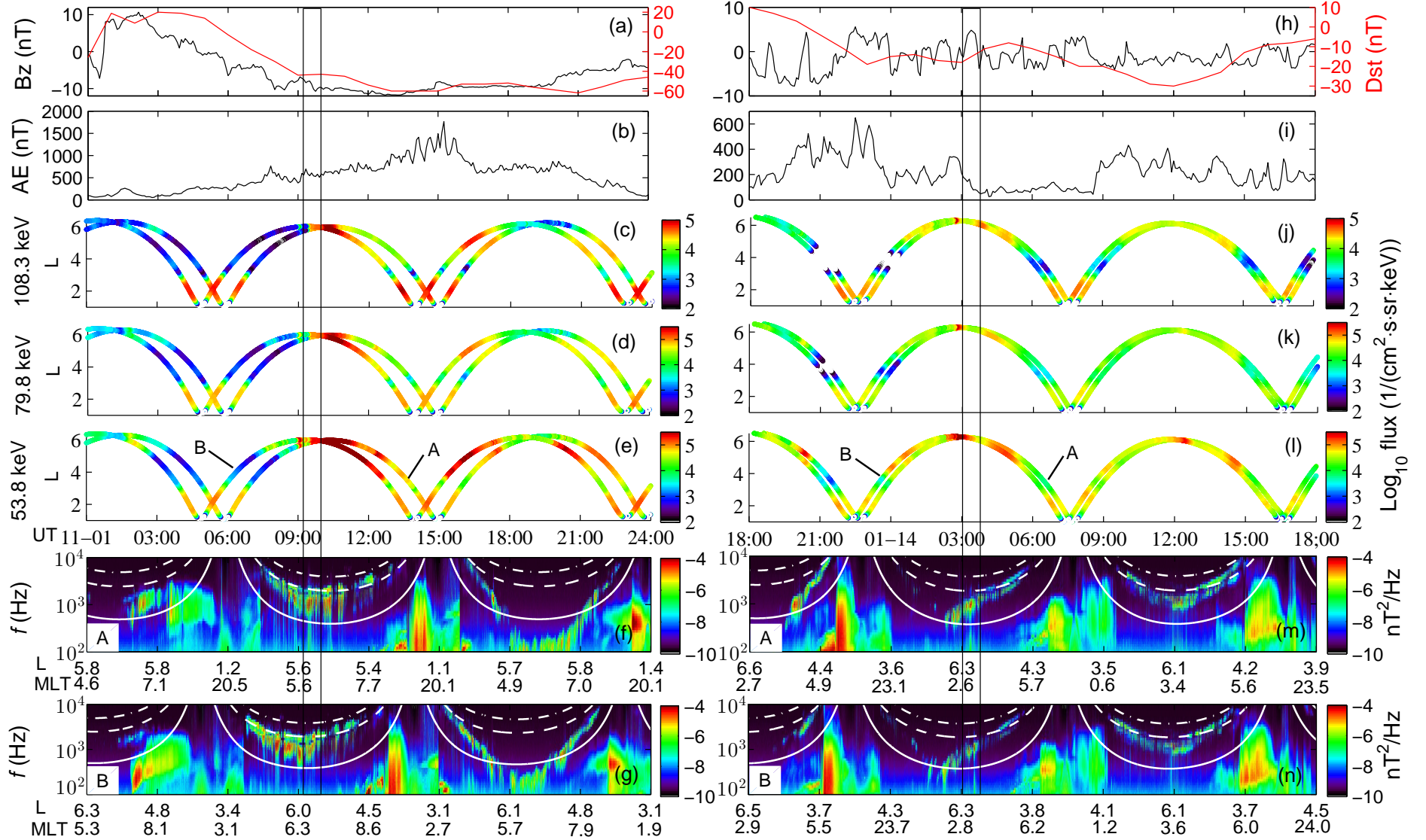
Figure 11. Ray paths for different wave parameters (shown), launched at locations (pentagrams) $L = 6.3$ and 6.1 for Probes A and B. The dashed and dotted lines indicate the plasmopause, and field lines with the invariant latitudes: 65° and 67° .

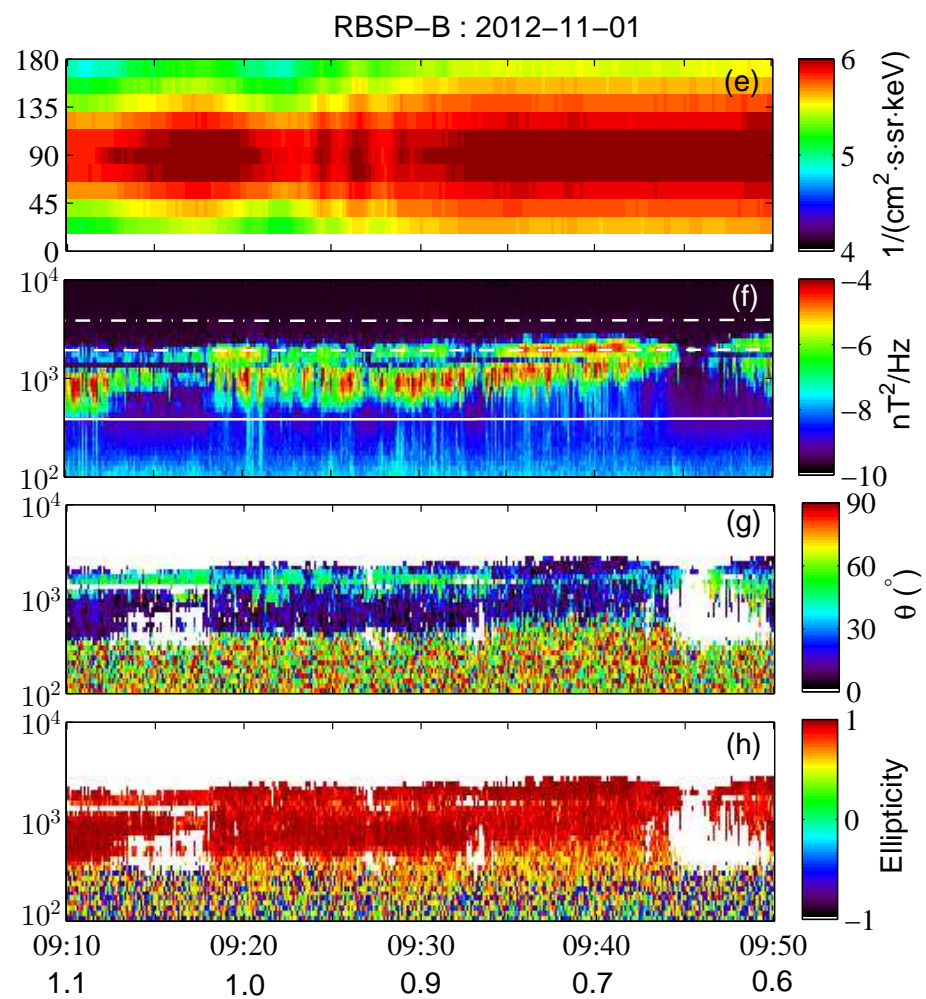
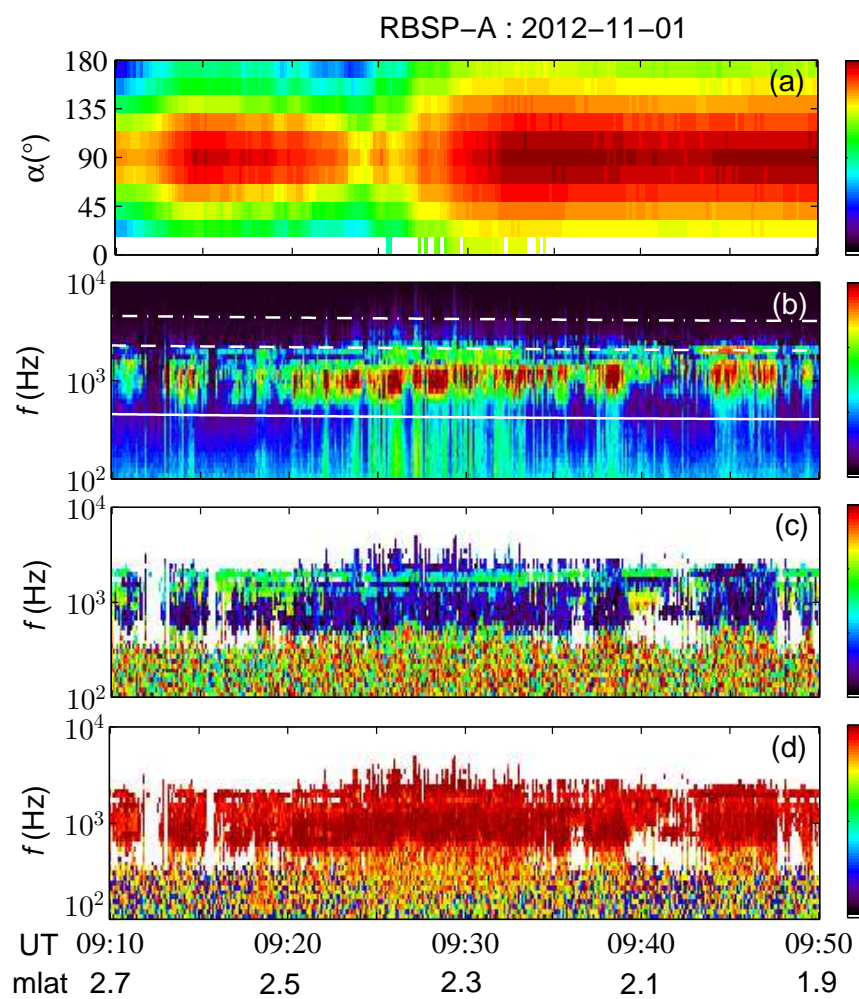
Figure 12. Van Allen Probe data on 8 May 2014. (a) The IMF Bz (black) and the Dst index (red). (b) The AE index. (c) Pitch angle distributions of energetic electron fluxes in unit of \log_{10} . (d) Wave magnetic field spectral density (in unit of \log_{10}). The white lines represent $0.1f_{ce}$ (solid), $0.5f_{ce}$ (dashed) and f_{ce} (dot-dashed). (e) Wave normal angle. (f) Wave ellipticity. The pair of vertical lines indicate the simulation periods: 09:50-10:30 UT.

Figure 13. (upper) Modeled bi-Maxwellian distribution (solid) to the observed electron PSD (discrete) for $v_{\perp} = 0$ (blue) and $v_{\parallel} = 0$ (red). (lower) The corresponding scaled local growth rate γ/Ω_{ce} as a function of wave frequency ω at the initial azimuthal angle $\eta = 0^{\circ}$ and different initial wave normal angles (shown).

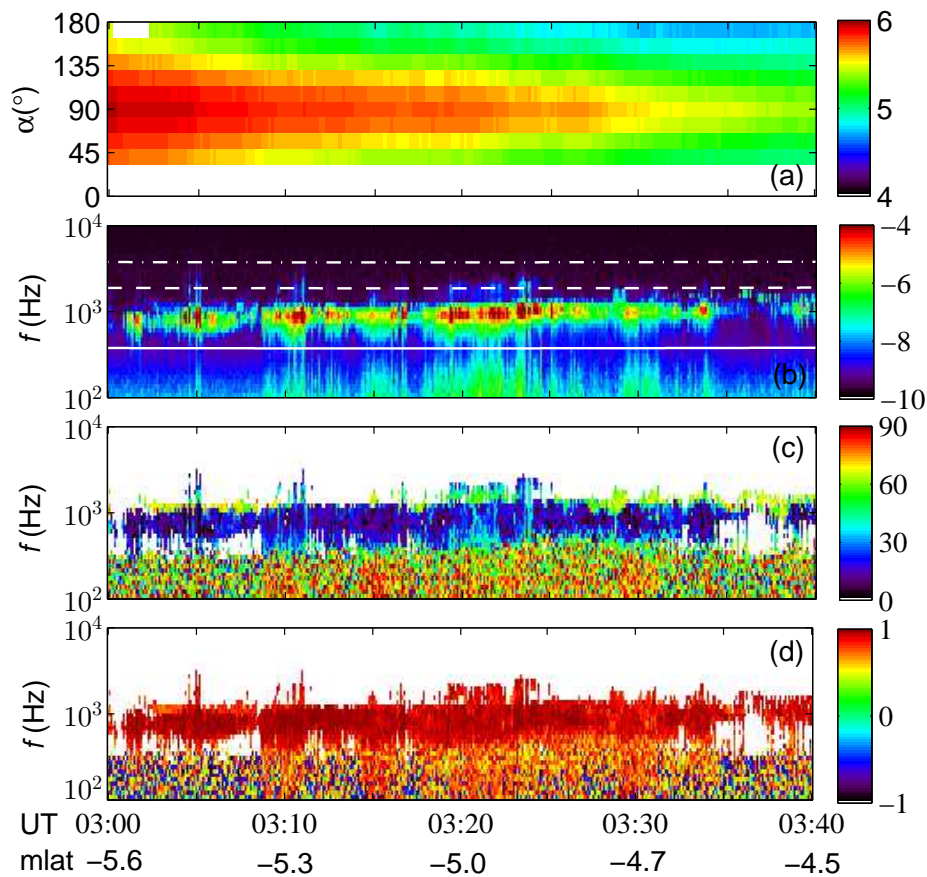
Storm A: 2012-11-01

Storm B: 2013-01-13 ~ 2013-01-14

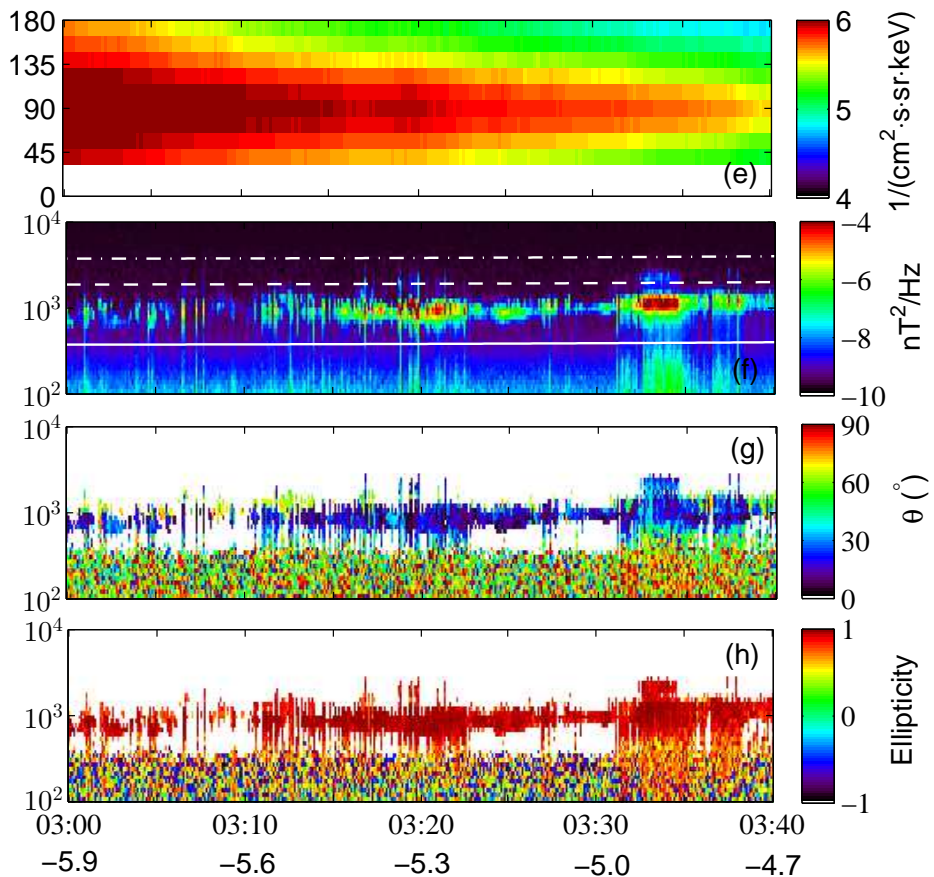




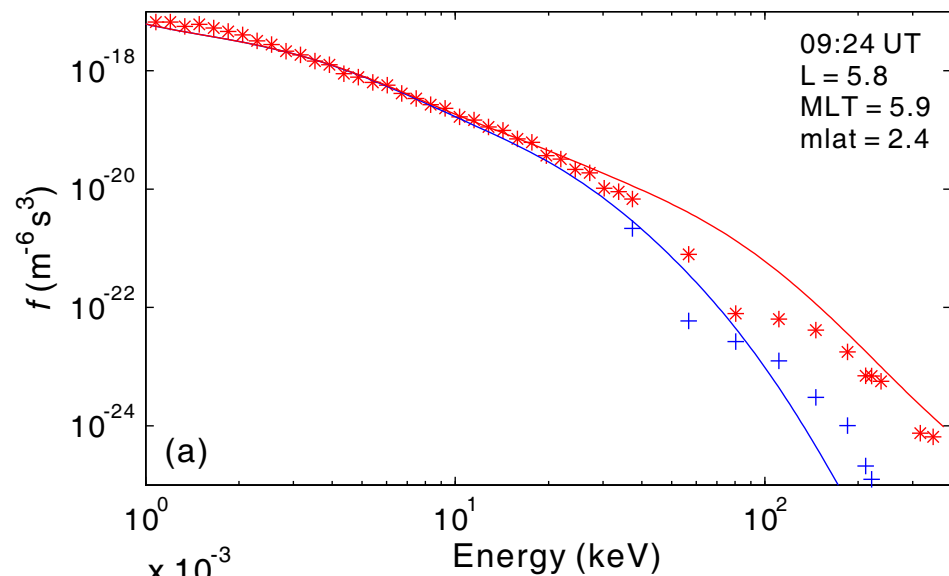
RBSP-A : 2013-01-14



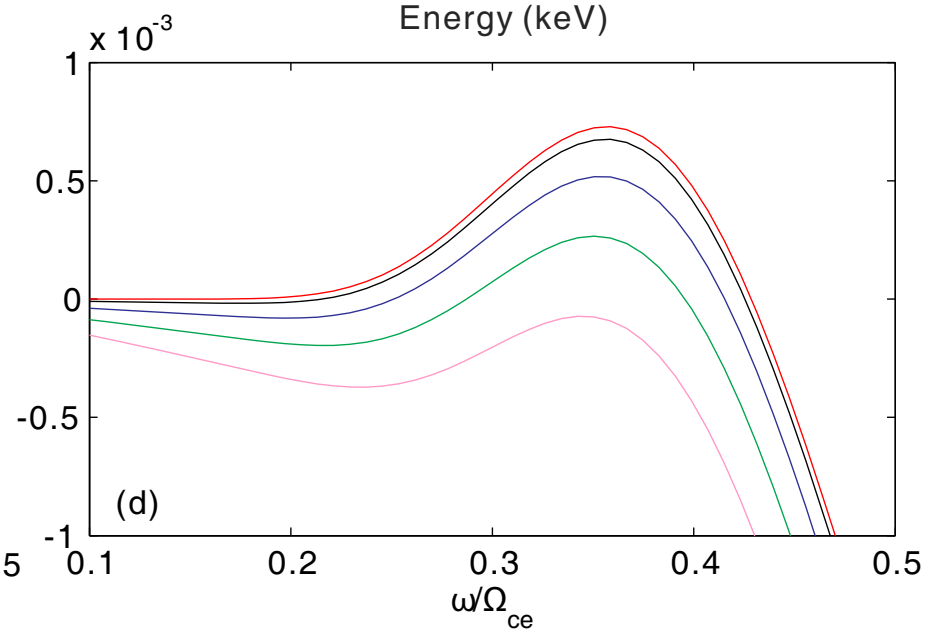
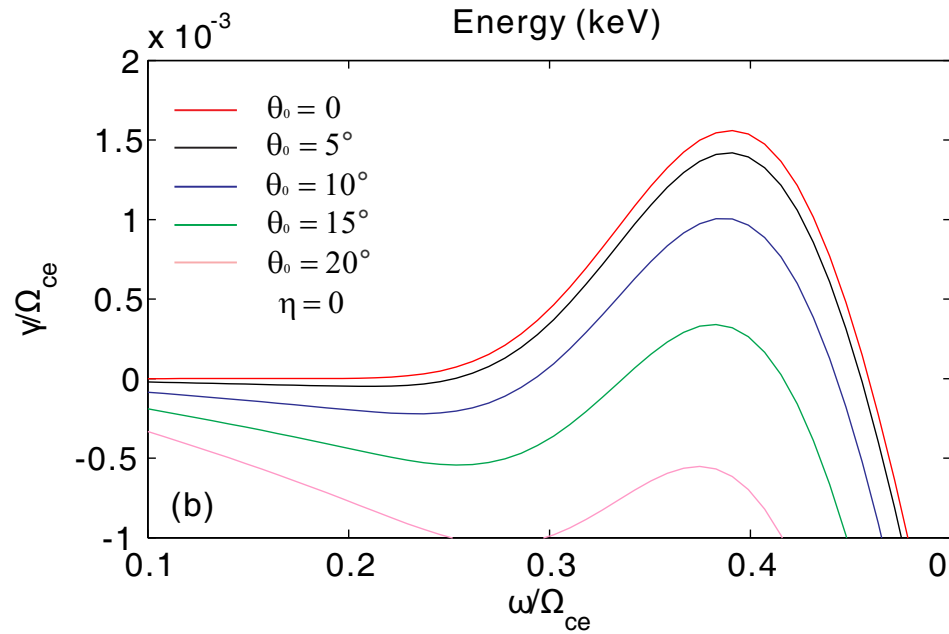
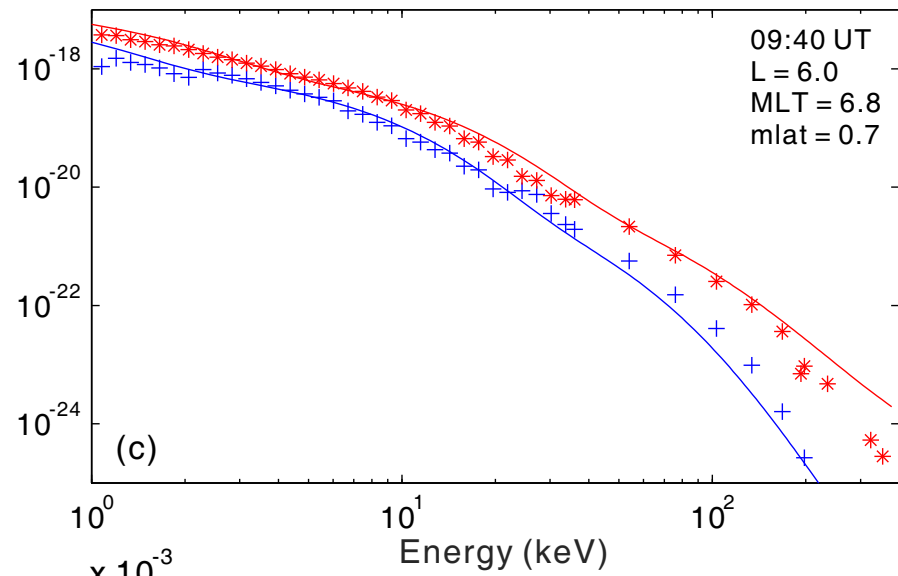
RBSP-B : 2013-01-14



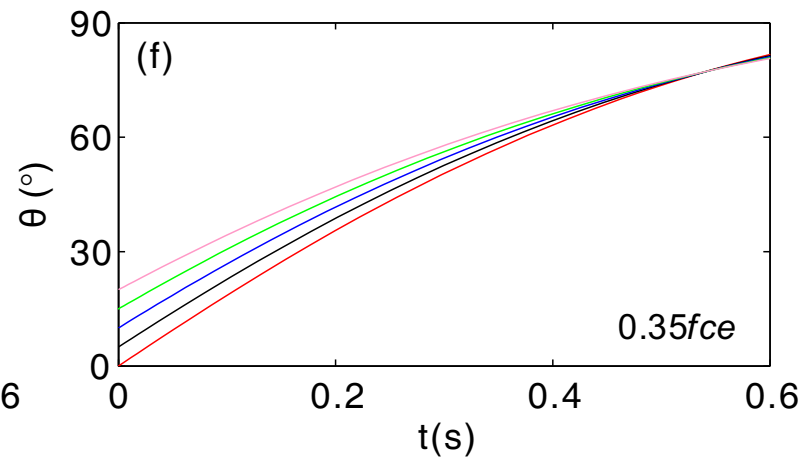
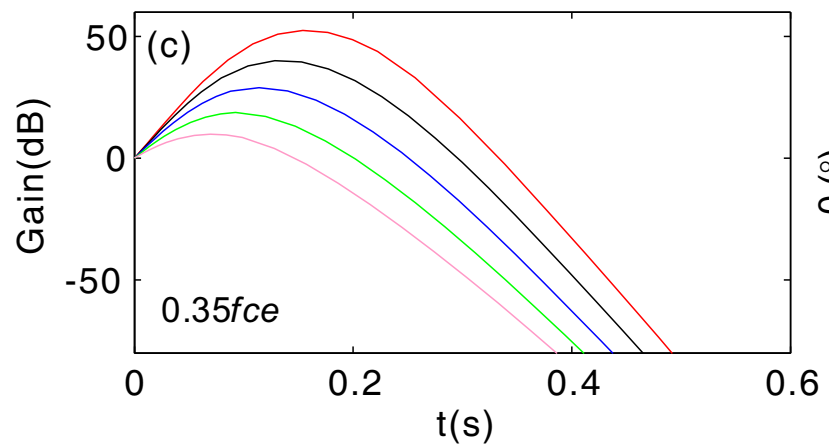
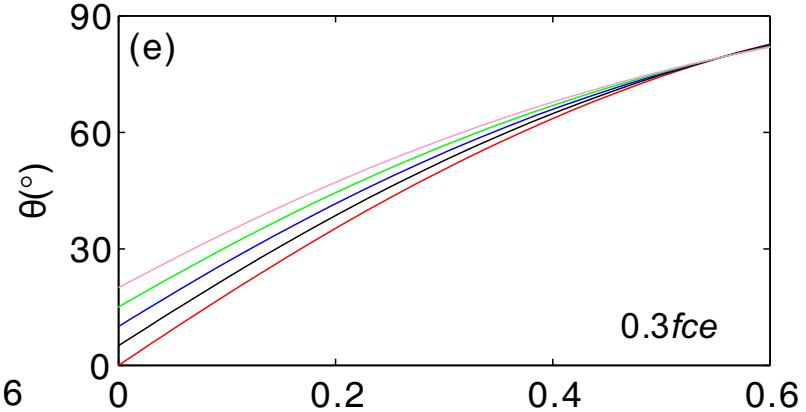
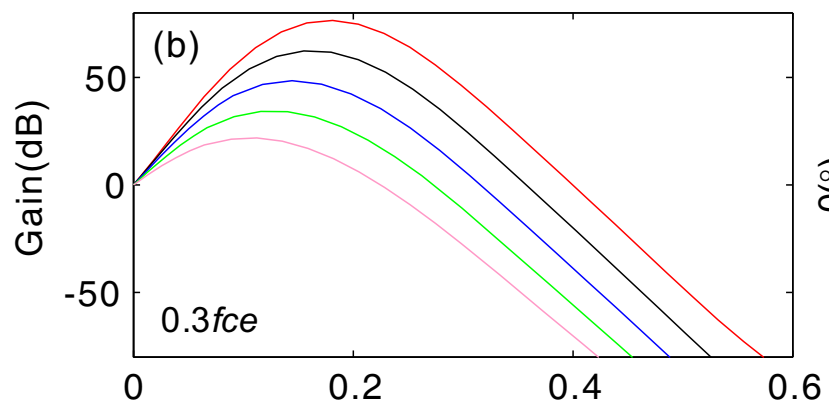
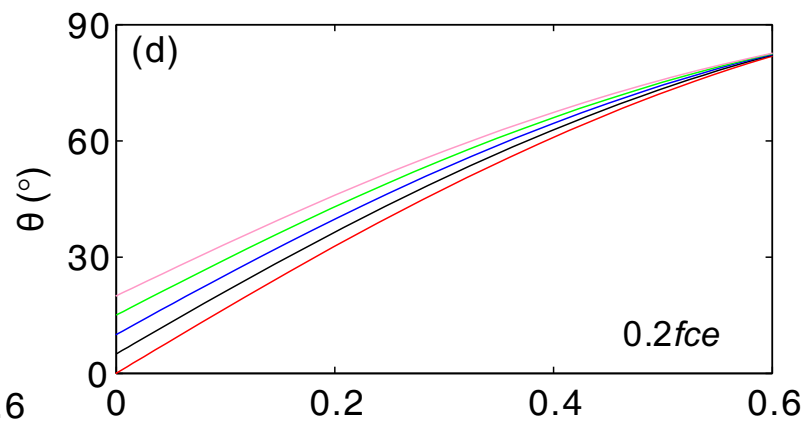
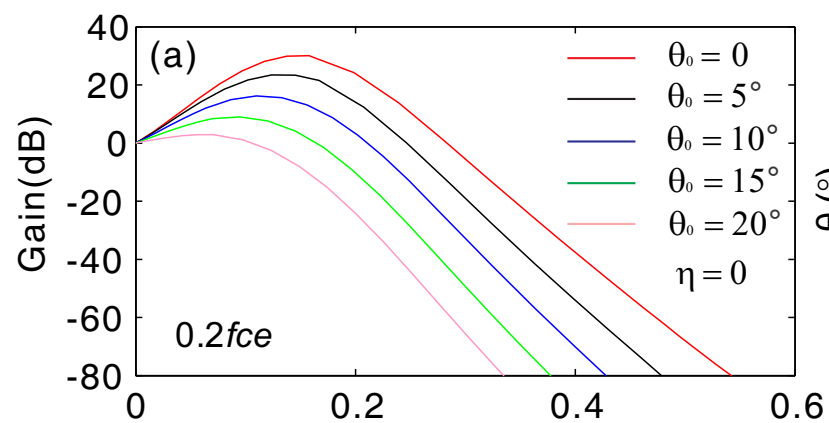
RBSP-A: 2012-11-01



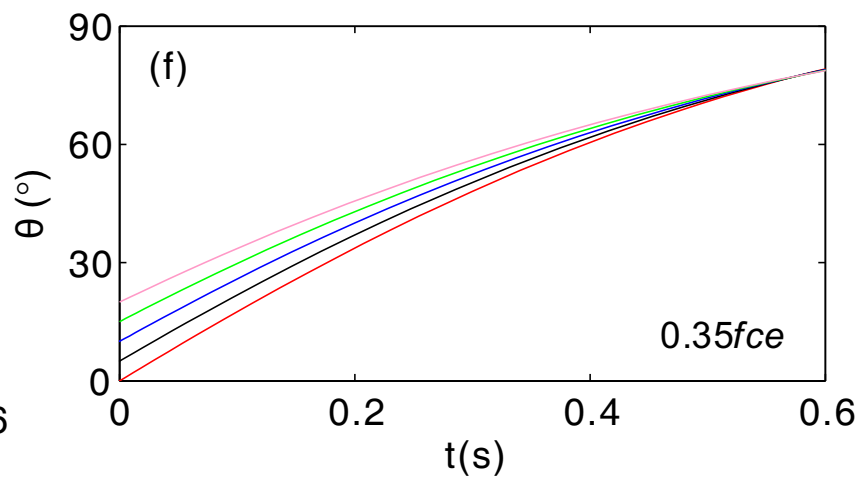
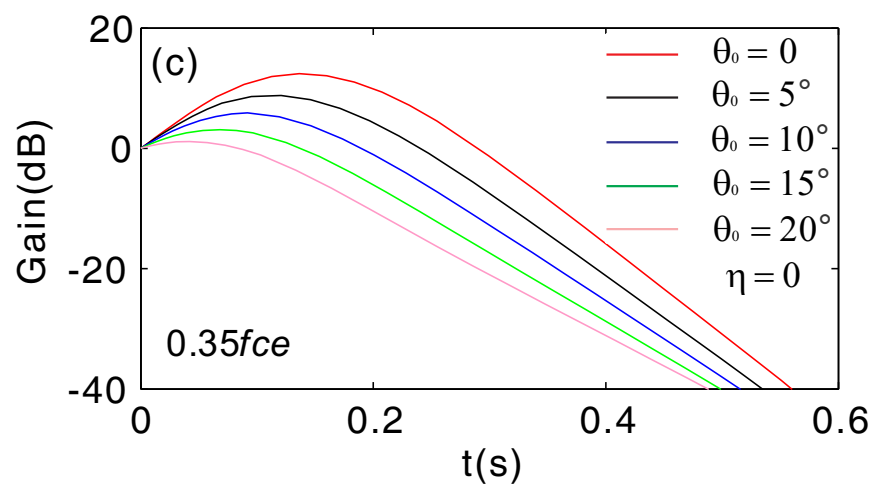
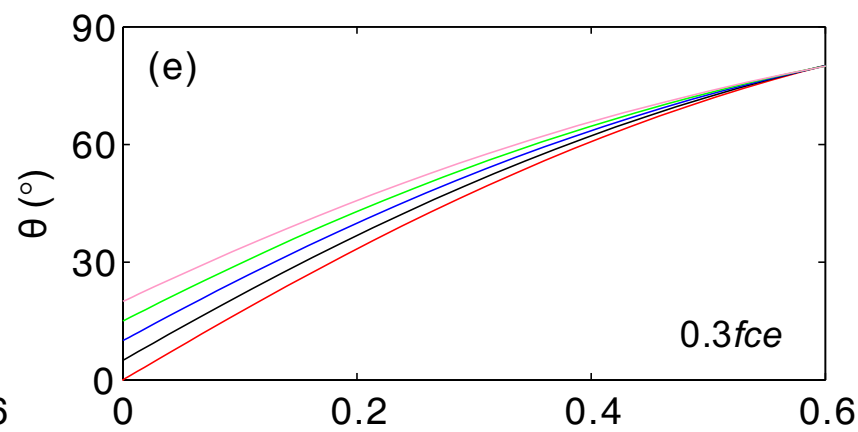
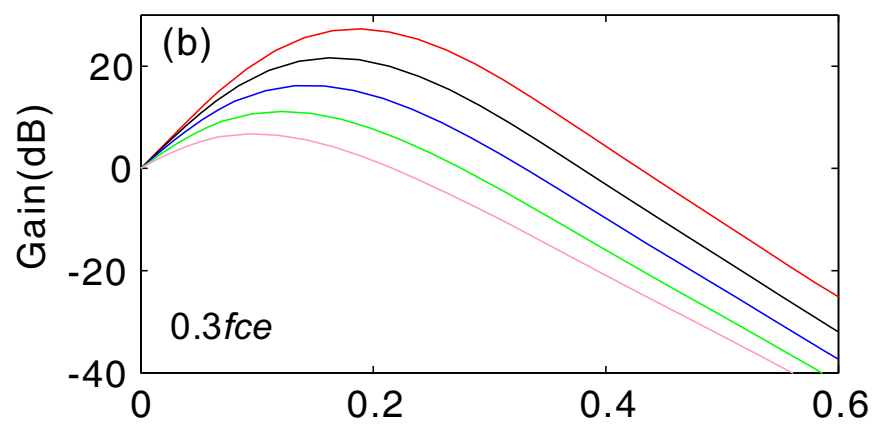
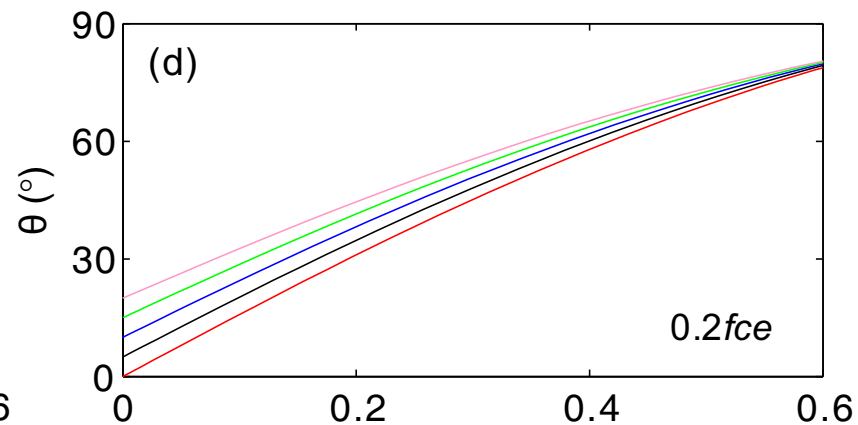
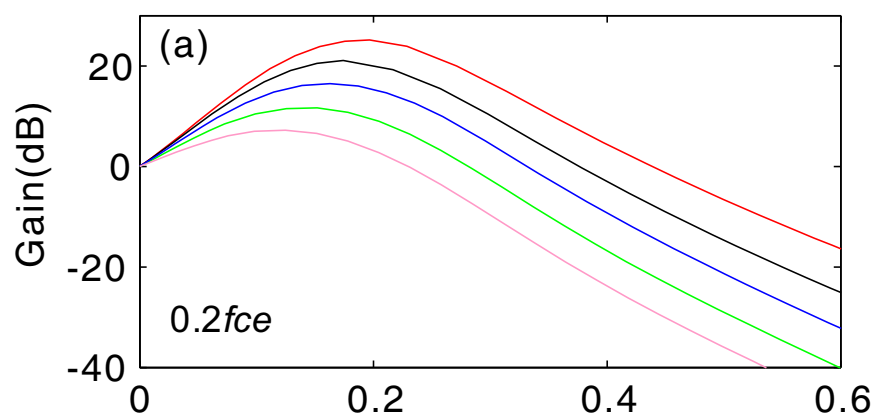
RBSP-B: 2012-11-01



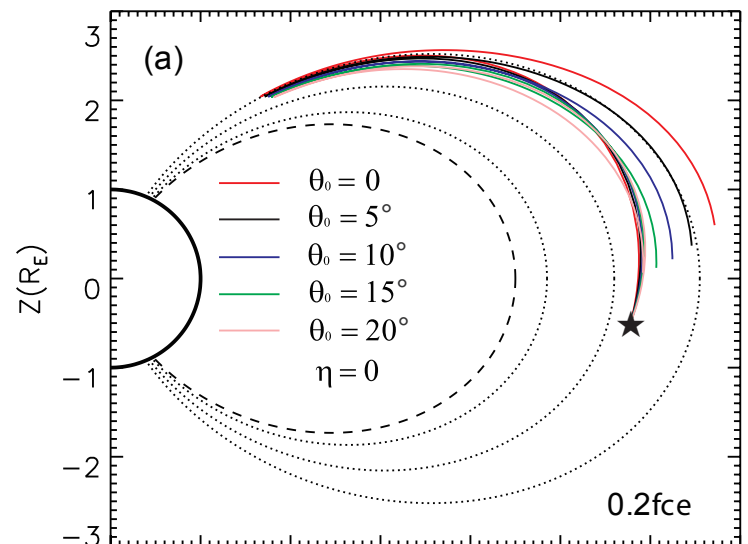
RBSP-A: 2012-11-01



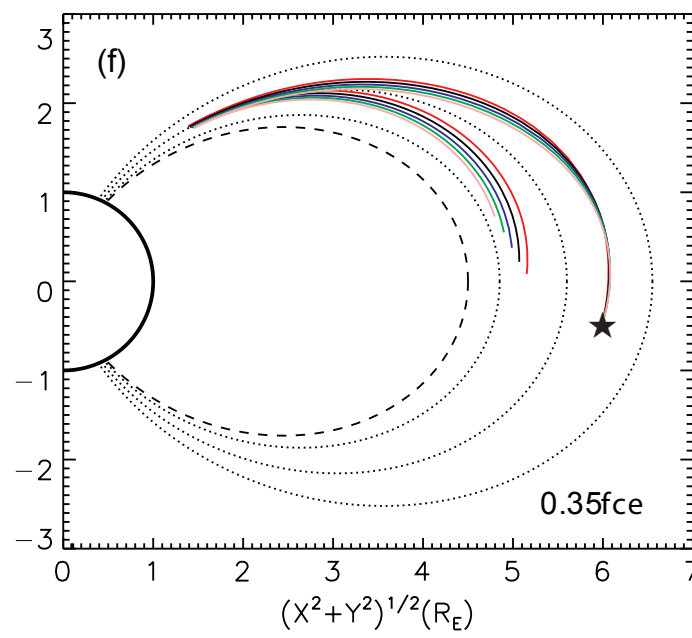
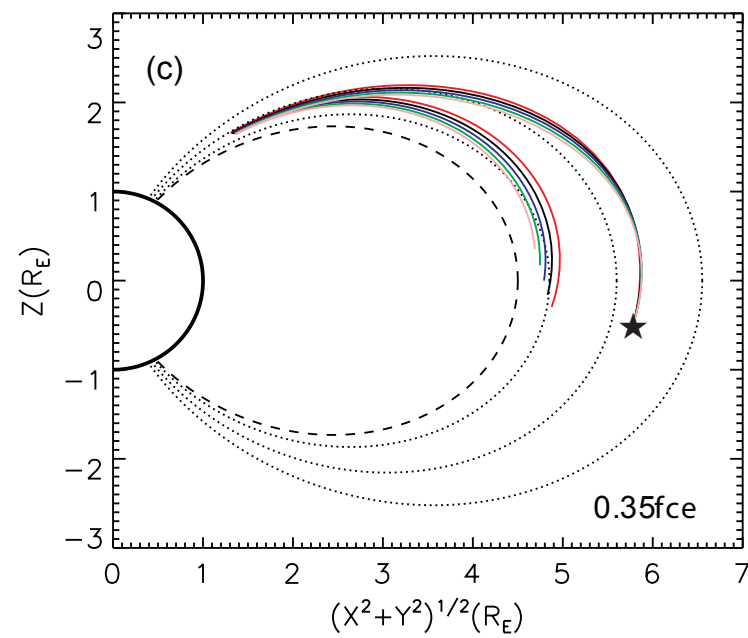
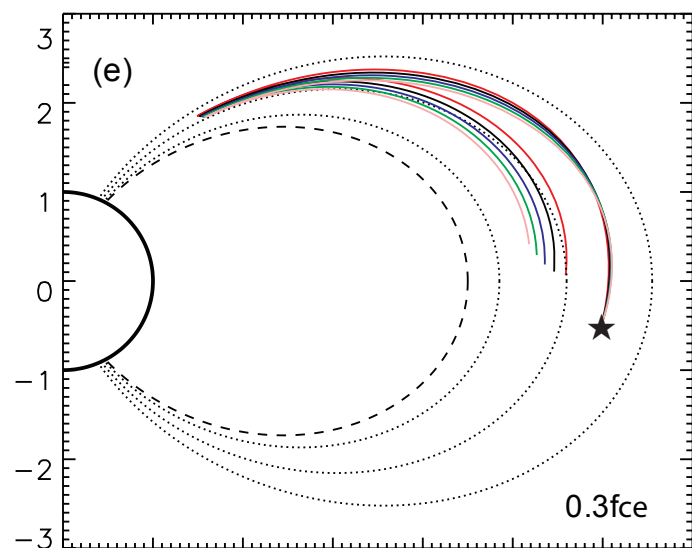
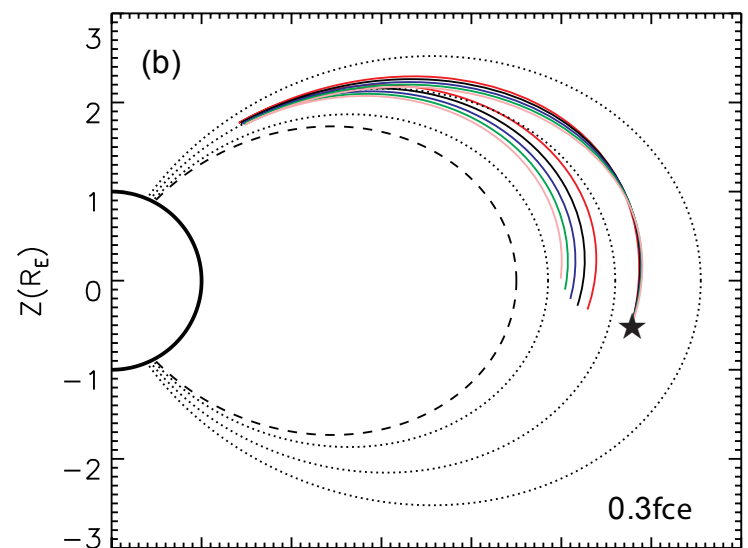
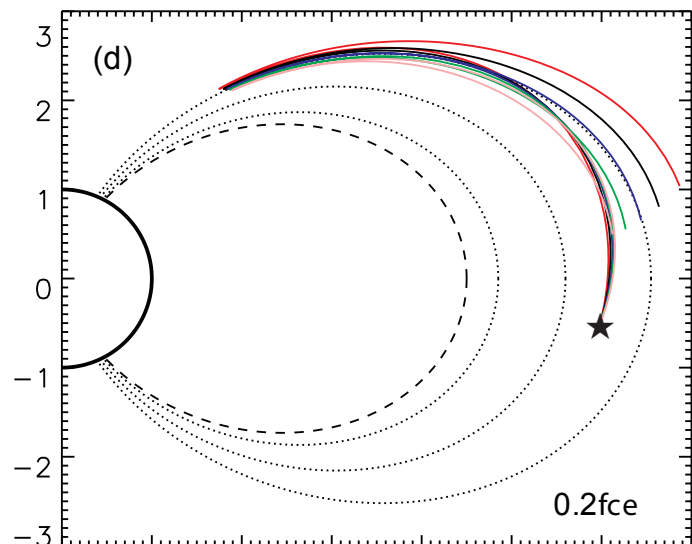
RBSP-B: 2012-11-01



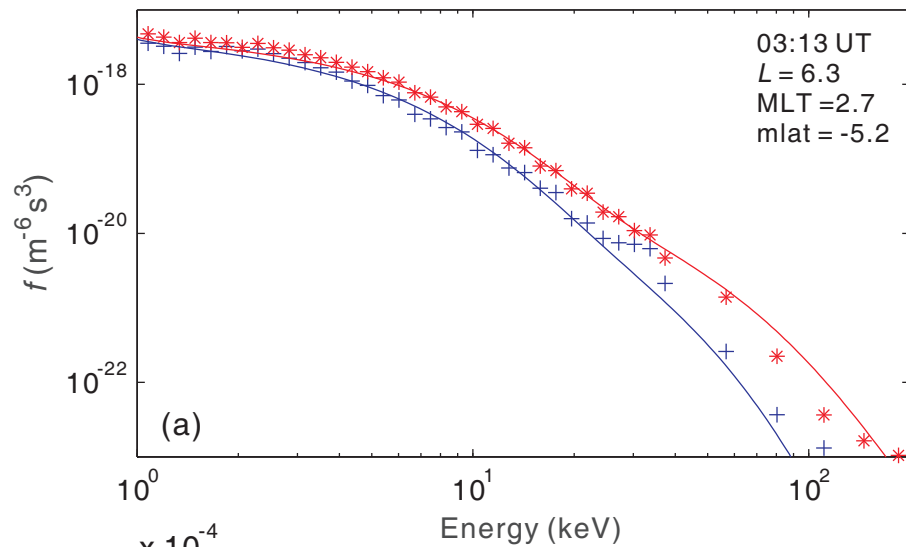
RBSP-A: 2012-11-01



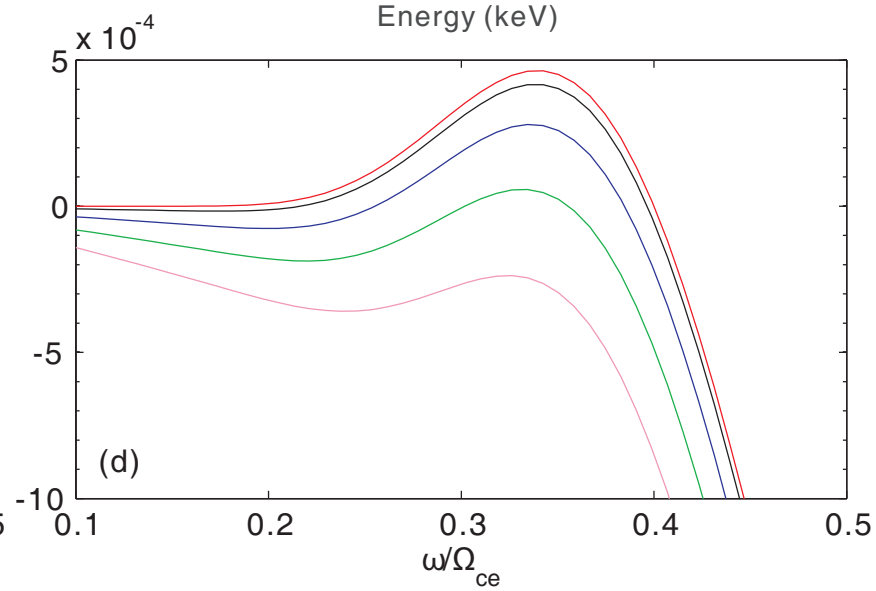
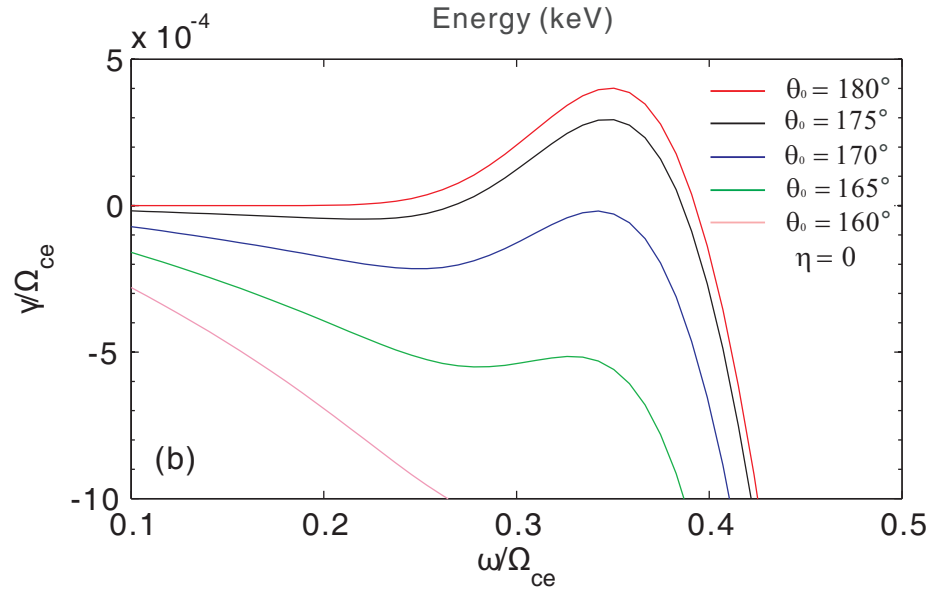
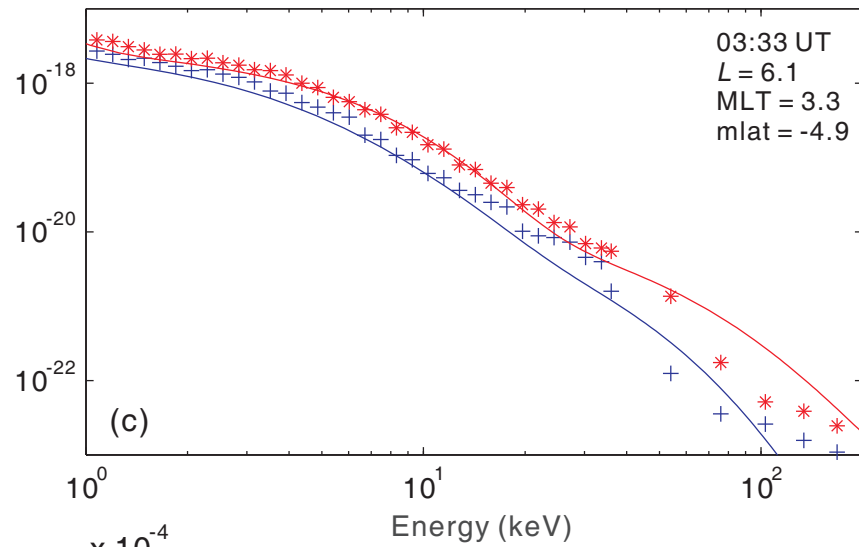
RBSP-B: 2012-11-01

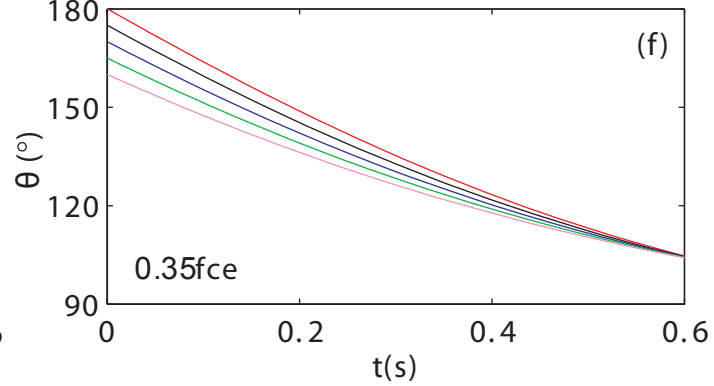
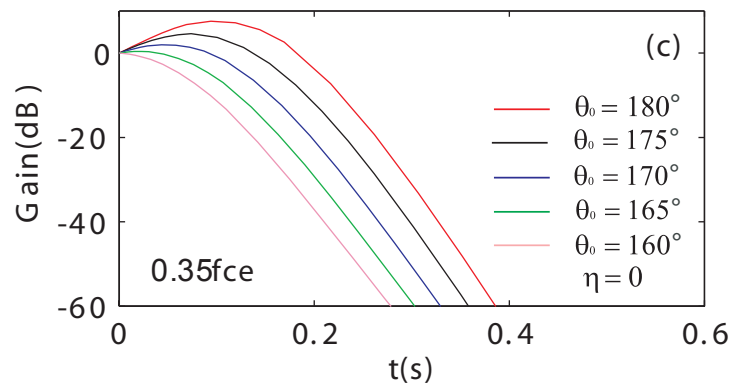
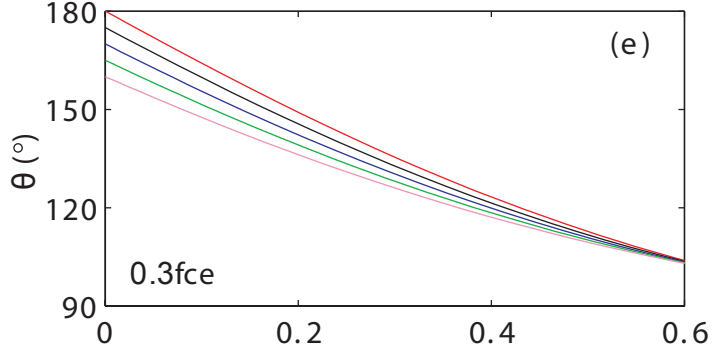
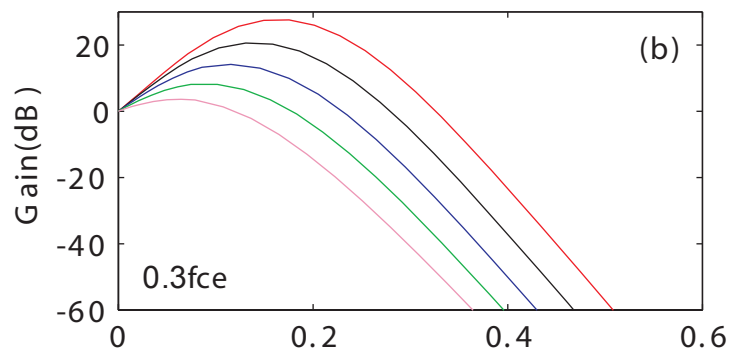
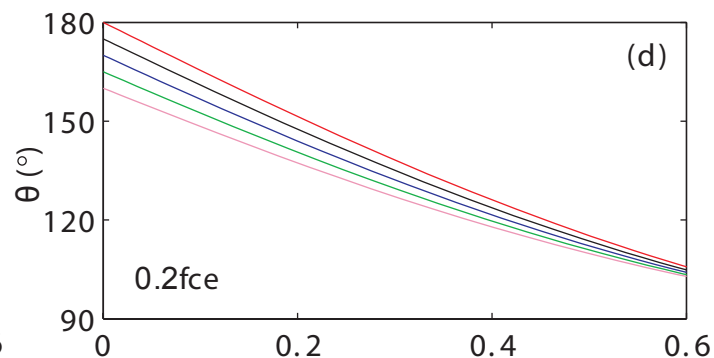
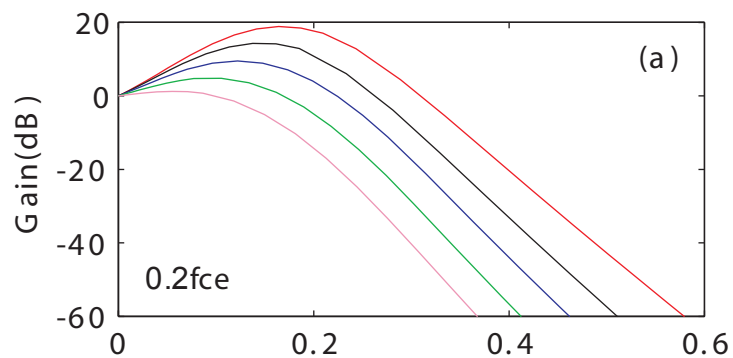


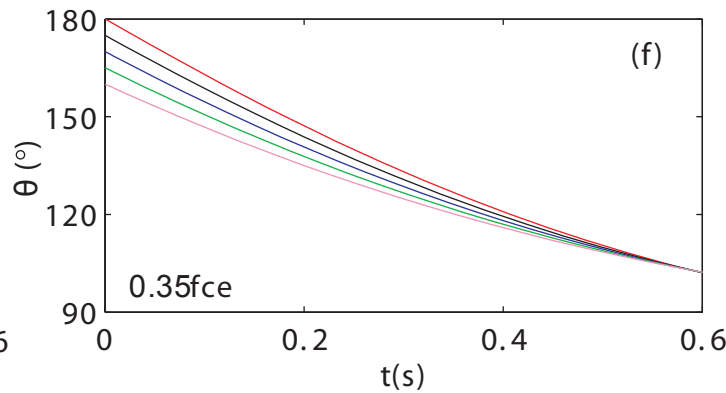
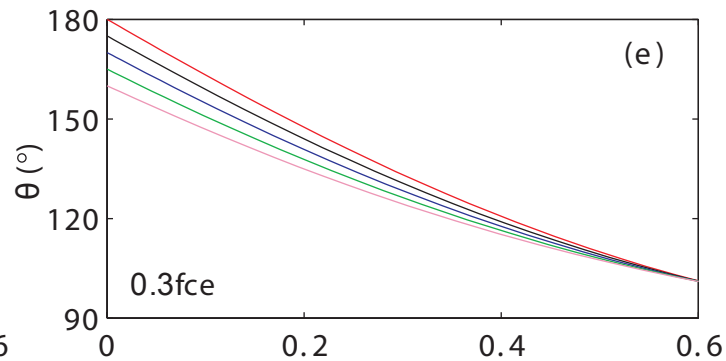
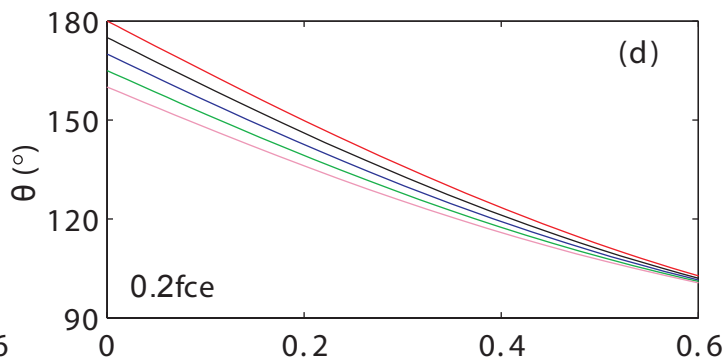
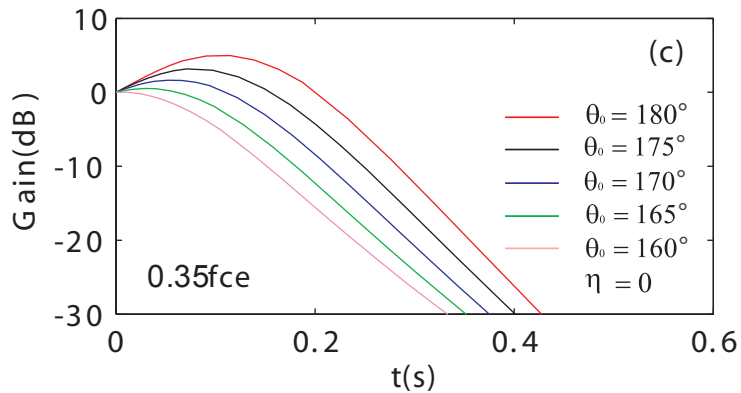
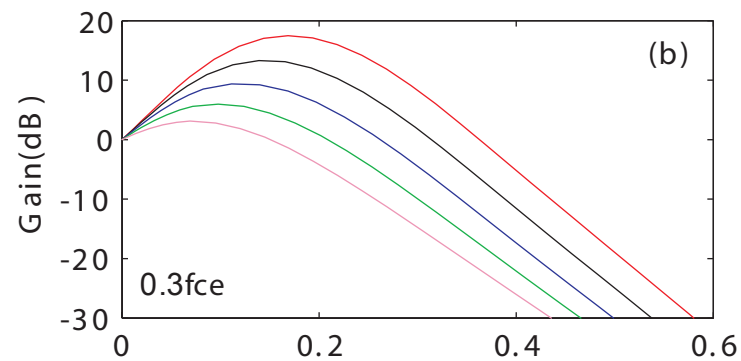
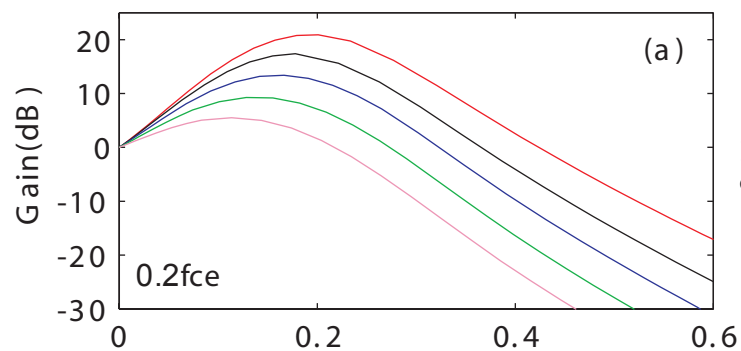
RBSP-A: 2013-01-14



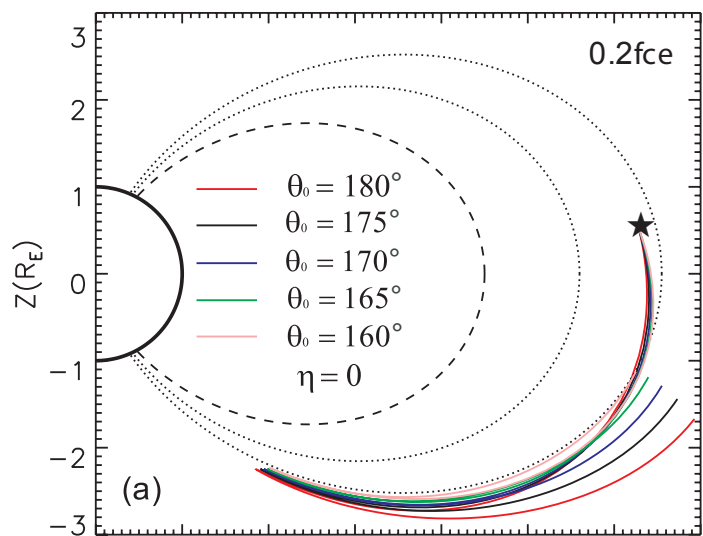
RBSP-B: 2013-01-14



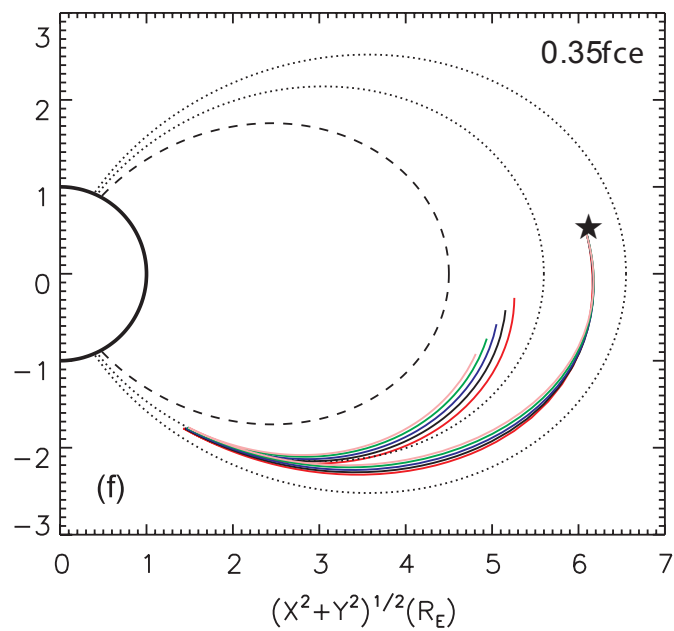
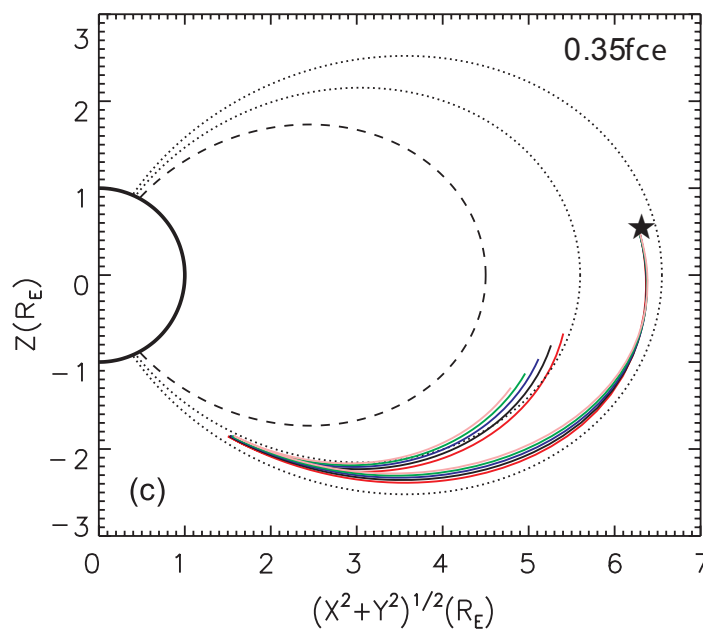
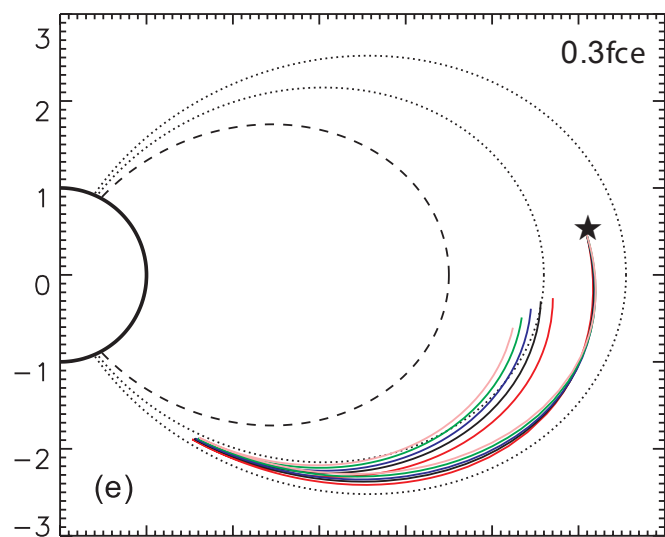
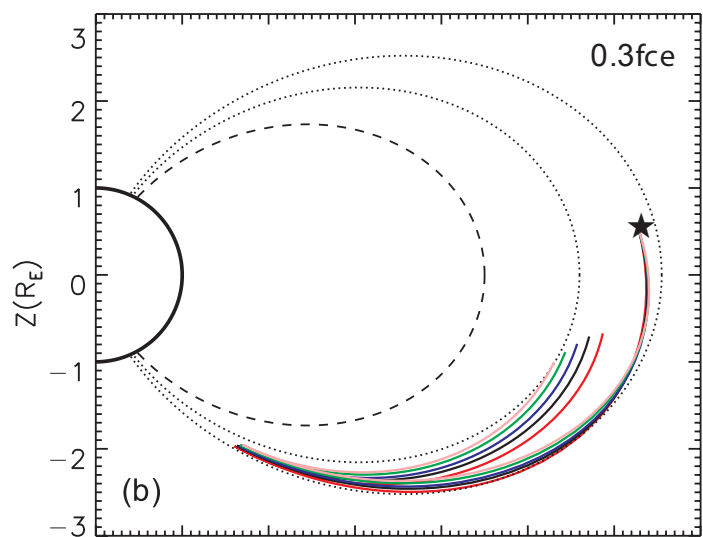
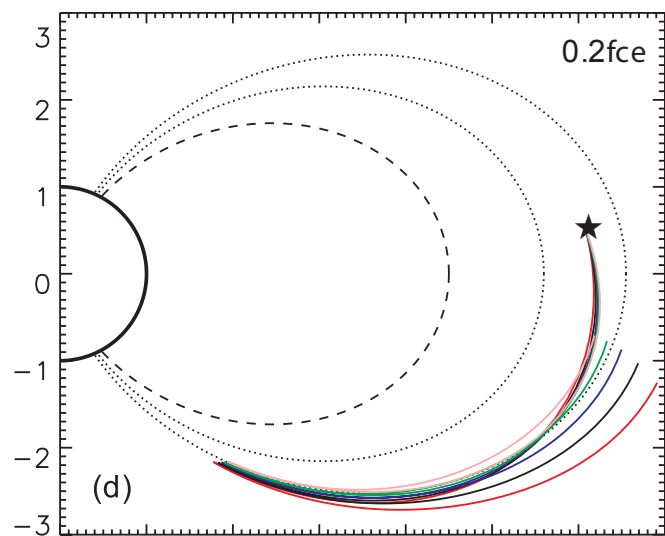


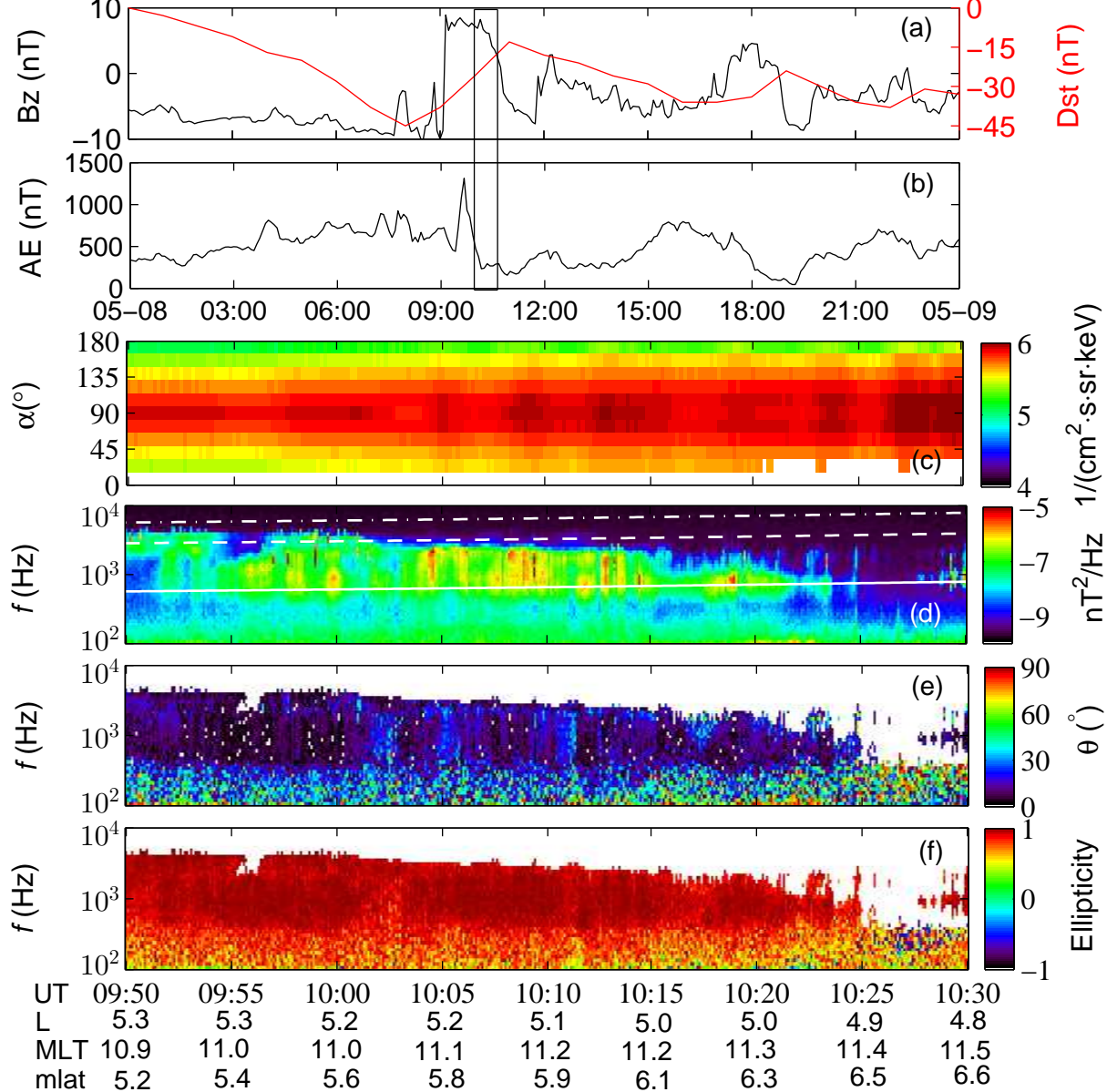


RBSP-A: 2013-01-14



RBSP-B: 2013-01-14





RBSP-B: 2014-05-08

